

A CdS/CdSeTe with Carbon Nanospheres Sensitized Solar Cell with a Reduced Graphene Oxide Counter Electrode: Fabrication and Characterization

A Project Report Submitted
as part of the requirements for the degree of

MASTER OF SCIENCE

By

SUBHAJIT LAHA

(Roll No. CY 13M1014)

Under the supervision of

Dr. M. Deepa



to the
DEPARTMENT OF CHEMISTRY
INDIAN INSTITUTE OF TECHNOLOGY HYDERABAD
INDIA

APRIL, 2015

Declaration

I hereby declare that the matter embodied in this report is the result of investigation carried out by me in the Department of Chemistry, Indian Institute of Technology Hyderabad under the supervision of Dr. M. Deepa

In keeping with general practice of reporting scientific observations, due acknowledgement has been made wherever the work described is based on the findings of other investigators.

Subhajit Laha 29.09.2015

(Signature)

Subhajit Laha

(Student Name)

CY13M1014

(Roll No.)



Signature of the Supervisor

Dr. M. Deepa

Department of Chemistry

Indian Institute of Technology Hyderabad

Ordnance Factory Campus,

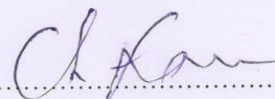
Yeddumailaram 502205, Telengana

India

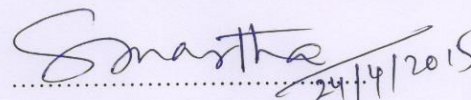
Dr. M. Deepa
Assistant Professor
Department of Chemistry
Indian Institute of Technology Hyderabad
Ordnance Factory Estate
Yeddumailaram-502 205
Andhra Pradesh, India

Approval Sheet

This thesis entitled "A CdS/CdSeTe with Carbon Nanospheres Sensitized Solar Cell with a Reduced Graphene Oxide Counter Electrode: Fabrication and Characterization" by Subhajit Laha is approved for the degree of Master of Science from Indian Institute of Technology Hyderabad.



Name and affiliation
Examiner



Name and affiliation
Examiner

Surendra K. Martho
Assistant Professor
Dept. of Chemistry

Dr. M. Deepa
Assistant Professor
Department of Chemistry
Indian Institute of Technology Hyderabad
Ordnance Factory Estate
Maidamallaram-502 205
Telangana Pradesh, India



Name and affiliation
Advisor

Name and affiliation
Chairman

Acknowledgements

I take this opportunity to express my profound gratitude and deep regards to my respectful supervisor, **Dr. M. Deepa** for her exemplary guidance, monitoring and constant encouragement throughout the course of this project. The blessing, help and guidance given by her time to time shall carry me a long way in the journey of life on which I am about to embark. Hereby I include the notion of confidence that she has bestowed upon me by including me in her group requires no elaboration and I feel very much privileged in working under such an esteemed, eminent and masterly guide without whom compilation of this present form would be mere impossible. Particularly I am very thankful to her for creating an intense interest on this field of research. I wish to thank Mr. P. Naresh Kumar for assisting and accompanying me in due course of time with his thoughts and intuition. I am extremely thankful to Mr. S. Rambabu, Mr. A. Bhaskar, Mr. B. Narasimha Reddy, Mrs. Radha, Mr. Ramesh Kokal and Ms. Aparajita Das for their help throughout in learning experimental techniques, inspiring and invaluable conceptual understandings that have benefited me during the course of the project.

I want to thank Department of Chemistry and IIT Hyderabad for providing basic infrastructure and extending all the necessary facilities.

I am thankful to my classmates, for their constant company throughout the project. I am in sort of words in expressing my heart full thanks to my parents constant support encouragement and for motivating me in the field of Chemistry.

Abstract:

To make Quantum Dot Sensitized Solar Cells (QDSSCs) competitive, it is necessary to achieve power conversion efficiencies comparable to other solar cell technologies. In this work, a photoactive electrode consisting of CdS (visible light absorbing) and CdSeTe (alloyed quantum dots with an excitonic absorption onset at 859 nm) and Carbon Nanospheres (CNS) were prepared by assembling them onto a mesoporous TiO₂ electrode for the first time. Carbon Nanospheres were prepared from starch by an acid treatment and they were dissolved in ethanol and deposited onto TiO₂ electrophoretically. CdS QDs were formed over TiO₂ and the TiO₂/CNS electrodes by SILAR (Successive Ionic Layer Absorption and Reaction) method and CdSeTe QDs were deposited over them by an electrophoretic deposition method. Both the electrodes (photoanode and cathode) were characterized by electron microscopy, cyclic voltammetry, Raman and X-ray diffraction analyses. QDSSCs were constructed with photoanodes of different compositions, and with a 0.1 M Na₂S in water-methanol (3:7) solution as electrolyte and a Reduced Graphene oxide based counter electrode. The best overall power conversion efficiency was achieved for the TiO₂/CNS/CdS/CdSeTe photoanode-based cell and it is 2.82%. The use of a near-infrared absorber like CdSeTe and electron acceptors like Carbon nanospheres in realizing remarkable improvements in solar-cell performance metrics is demonstrated.

Table of Contents

1.Introduction	(11)
1. a. Materials required for Solar cell	(12)
1. b. Photovoltaic effect	(13)
1. c. Types of Solar cells	(13)
1. c. 1. Silicon cells	(13)
1. c. c. 1. Single-crystalline silicon cells	(14)
1. c. c. 2. Multi-crystalline silicon cells	(14)
1. c. 2. Thin film solar cell	(14)
1. c. 3. Polymer solar cell	(14)
1. c. 4. Dye Sensitized solar cell	(15)
1. c. 2. a. Advantages	(16)
1. c. 2. b. Disadvantages	(16)
1. c. 3. Quantum dot sensitized solar cell	(17)
1. c. 3. 1. Quantum Dot	(17)
1. c. 3. 1. a. Core-Type Quantum Dots	(18)
1. c. 3. 1. b. Core-Shell Quantum Dots	(18)
1. c. 3. 1. c. Allowed Quantum Dots	(18)
1. c. 3. 2. Quantum Confinement	(18)
1. c. 3. 3. Parameters of QDSSCs	(19)
1. c. 3. 3. a. IV curve of Solar Cell	(19)
1. c. 3. 3. b. Short-circuit Current	(20)

1. c. 3. 3. c. The open-circuit voltage	(20)
1. c. 3. 3. d. Fill Factor	(20)
1. c. 3. 3. e. Efficiency	(21)
1. c. 3. 4. Working mechanism of QDSSCs	(21)
1. c. 3. 5. Advantages over DSSC	(22)
1. c. 3. 6. Deposition of semiconductor QDs over mesoscopic TiO ₂ film	(22)
1. c. 3. 7. Recent trends of CdSeTe based on QDSSCs	(24)
2. Experimental details	(25)
2. 1. Chemicals	(25)
2. 1. 1. Preperation of CdSe _x Te _{1-x}	(25)
2. 1. 2. Preperation of Carbon Nanospheres	(26)
2. 3. Preperation and reduction of Graphite Oxide (GO)	(26)
2. 2. Fabrication of Photoanode	(27)
2. 4. Fabrication of Counter Electrode	(27)
2. 5. Electrolyte	(27)
3. Result and Discussion	(28)
3. 1. UV-Visible spectroscopy analysis	(28)
3. 2. Cyclic Voltammetric analysis	(29)
3. 3. XRD analysis	(30)
3. 4. SEM analysis	(32)
3. 5. Determination of Equilibrated Fermi level of Carbon Nanospheres	(34)

3. 6. Determination of conductivity by Linear Sweep Voltammetry analysis	(36)
3. 7. Mott-Schottky analysis	(36)
3. 8. FTIR spectroscopic analysis of RGO	(38)
3. 9. Raman spectroscopy analysis of GO and RGO	(39)
3. 10. Fluorescence spectral analysis	(40)
3. 11. Impedance measurement and determination of back electron transfer for all the cells	(41)
3. 12. Energy Band diagram	(44)
3. 13. J-V Characteristics	(45)
4. Conclusion	(46)
5. References	(46)

List of Figures

Figure 1.a: That solar energy is the only choice that can satisfy such a huge and steadily increasing demand among the all others renewable energy sources. (12)

Figure 1.b: Difference in grain size and techniques for various types of silicon cells. (13)

Figure 1.c: Schematic representation of working mechanism of DSSC. (16)

Figure 1.d: Density of states versus confinement. Here is shown the electronic density of states for different dimensionalities of confinement; a) bulk; b) 1D confinement, 2D material; c) 2D confinement, 1D material; d) 3D confinement, 0D material. (19)

Figure 1.e: Representation of I_{sc} and V_{oc} in characteristic $I-V$ curve. (20)

Figure 1.f: Schematic representation of working mechanism of QDSSC. (22)

Figure 1.g: Representation of different methods of QD deposition. (23)

Figure 1.h: Temporal evolution of J-V curves (a) and photovoltaic parameter values, η (b), J_{sc} , V_{oc} (c), and FF (d), for the CdSeTe₈₀₀ cells based on Cu₂S counter electrodes via electrode position of Cu on FTO glass. (25)

Figure 3.a: UV-Vis spectral analysis of (a) TiO₂, (b) CdS, (c) CdSeTe, (d) all the cells used as anode in solar cell. (28)

Figure 3.b: Cyclic voltammogram of (a) CdS (b) TiO₂ (c) CdSeTe. (29)

Figure 3.c: XRD patterns of (a) TiO₂ film, (b) CdS QDs film, (c) CdSeTe QDs film and (d) Carbon Nanosphere all on glass. (31)

Figure 3.d: XRD patterns of (a) Graphene oxide and (b) Reduced graphene oxide. (32)

Figure 3.e: SEM images of TiO₂, TiO₂ films have a granular porous morphology with pore sizes in the range of 25-175 nm. Such a porous structure is most advantageous for anchoring CdS and CdSeTe QDs through SILAR across the cross-section of TiO₂. (33)

Figure 3.f: SEM Image of Carbon Nanosphere with pore sizes in the range of 600-700 nm. (34)

Figure 3.g: Topography (a) and surface potential (b) maps of the CNS/FTO electrode. (35)

Figure 3.h: Linear sweep voltammograms of (a) Carbon Nanosphere and (b) Reduced graphene oxide; linear part of the each plot shown in the inset from where slope was calculated. (36)

Figure 3.i: Mott Schottky diagram (linear part is in inset) of Carbon Nanosphere and the image of CNS in acid solution filtrate after washing (left) before washing (right). (37)

Figure 3.j: FTIR spectra of (a) GO and (b) RGO. (38)

Figure 3.k: Raman spectra of (a) GO and (b) RGO. (39)

Figure 3.l: (a) a comparative fluorescence spectra of glass/CdS, FTO/CdS, FTO/TiO₂/CdS and FTO/TiO₂/CdS/CNS and (b) the fluorescence spectra of Carbon Nanosphere in ethanol solution

obtained at an excitation wavelength of 370 nm. It shows a broad peak from 430 nm to 460 nm range and the intensities of emission peaks are strong. (40)

Figure 3.m: (a) Nyquist plots recorded under an ac amplitude of 10 mV of Carbon Nanosphere and (b) Randles equivalent circuit used for fitting the experimental data. (41)

Figure 3.n: Nyquist plots recorded under an ac amplitude of 20 mV and under V_{OC} for photoelectrochemical solar cells with (a) $TiO_2/CdSeTe$, (b) $TiO_2/CdSeTe/CNS$, (c) $TiO_2/CdS/CNS$, (d) TiO_2/CdS , (e) $TiO_2/CdS/CdSeTe/CNS$, and (f) $TiO_2/CdS/CdSeTe$ as photoanode and Reduced graphene oxide as counter electrode under 0.1 M Na_2S in ultrapure water-methanol 3:7 (v/v) solution was employed as the electrolyte. (42)

Figure 3.o: A plot of phase vs log of frequency (ν) for all the cells used as photoanode. (42)

Figure 3.p: Energy band diagram of $FTO/TiO_2/CNS/CdS/CdSeTe$ showing the various electron transfer modes. (44)

Figure 3.q: The J-V characteristics of TiO_2/CdS , $TiO_2/CdSeTe$, $TiO_2/CdS/CNS$, $TiO_2/CdS/CdSeTe$ and $TiO_2/CdS/CdSeTe/CNS$. (45)

1. Introduction:

Solar energy in one form or another is the source of mostly all energy on this earth. Humans, like all other animals and plants, rely on the sun for warmth and food. However, people also harness the sun's energy in several other different ways. For example, fossil fuels, plant matter from a past geological age, is used for fuel and electricity generation and is essentially just stored solar energy from millions of years ago.

Photovoltaics by definition is a process of converting sunlight directly into electricity using solar cells. Today it is a rapidly growing and increasingly important renewable alternative to conventional fossil fuel electricity generation, but compared to other electricity generating technologies, it is a relative fresher, with the first practical photovoltaic devices demonstrated in the 1950s. Research and development of photovoltaics received its first major boost from the space industry in the 1960s which required a power supply separate from "grid" power for satellite applications. These space solar cells were several thousand times more expensive than they are today. The perceived need for an electricity generation method apart from grid power was still a decade away, but solar cells became an interesting scientific variation to the rapidly expanding silicon transistor development with several potentially specialized niche markets. Their application to the "remote" power supply area was quickly recognized and prompted the development of terrestrial photovoltaics industry. Small scale transportable applications (such as calculators and watches) were utilized and remote power applications began to benefit from photovoltaics [1].

1st generation solar cells: Traditional solar cells are made from silicon wafer-based solar cells.

2nd generation solar cells: Usually called thin-film solar cells because when compared to crystalline silicon based cells they are made from layers of semiconductor materials only a few micrometers thick.

3rd generation solar cells:

- Currently there is a lot of solar research going on in what is being referred to in the industry as 3rd generation solar cells.

- This new generation of solar cells are being made from variety of new materials besides silicon, including nanotubes, silicon wires and solar inks using conventional printing press technologies, organic dyes, and conductive plastics.
- Currently, most of the work on third generation solar cells is being done in the laboratory.
- The goal of course is to improve on the solar cells already commercially available – by making solar energy more efficient over a wider band of solar energy (e.g., including infrared), less expensive so it can be used by more and more people, and to develop more and different uses.

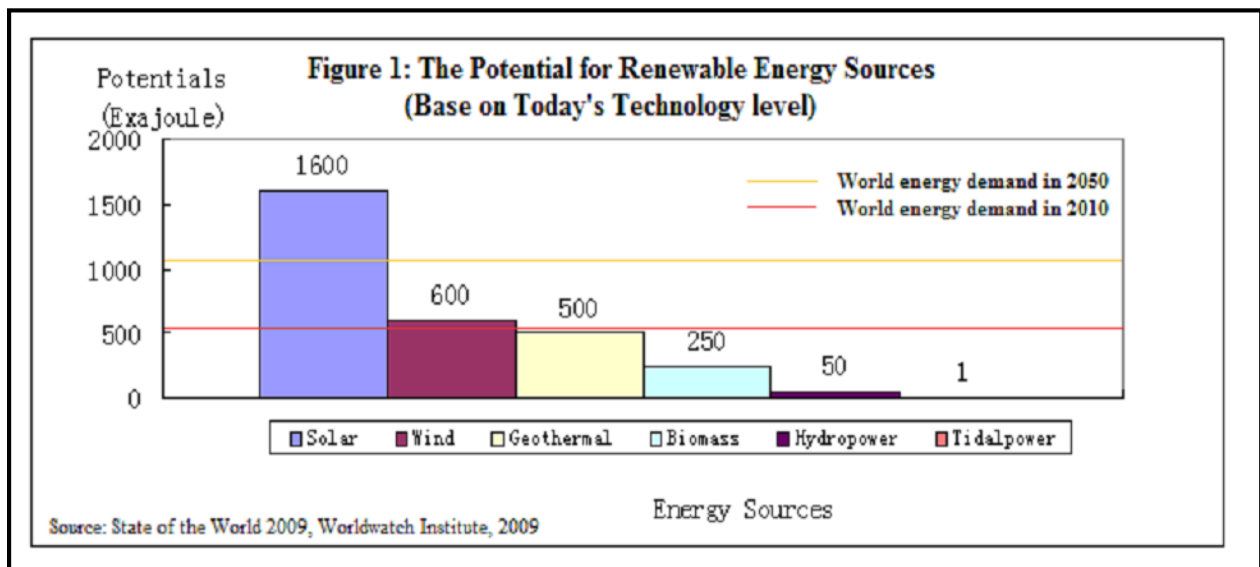


Figure 1.a: The solar energy is the only choice that can satisfy such a huge and steadily increasing demand among the all others renewable energy sources.

1. a. Materials required for Solar cell:

Most of the solar cells produced worldwide are composed of the semiconductor material Silicon (Si), as the second most abundant element in earth's crust. At first produce a solar cell in which, the semiconductor is "contaminated" or "doped". "Doping" is the introduction of chemical elements into the semiconductor. By doing this, depending upon the type of dopant, one can obtain a surplus of either positive charge carriers (p-type semiconductor) or negative charge carriers (n-type semiconductor layer). If two differently contaminated semiconductor layers are combined, then a so-called p-n-junction results on the boundary of the two layers. By doping trivalent

elements, we get p-type semiconductors (with excess amount of holes) and n-type semiconductors (with excess amount of electrons) are obtained by adding pentavalent elements.

In QDSSCs several important types of semiconductor nanomaterials (sensitizers such as CdS, Ag₂S, CdSe, CdTe, CdHgTe, InAs, PbSe, PbSSe, CuInS, CuInSe₂, CdSSe GaAs and PbS) [2] and other nanomaterials like TiO₂, ZnO, and carbon-based species are used. Understanding the mechanism of several photosensitization processes can provide design guidelines for future successful applications [3].

1. b. Photovoltaic effect:

In order to generate power, a voltage must be generated as well as a current. Voltage is generated in a solar cell by a process known as the "photovoltaic effect". The collection of light-generated carriers by the *p-n* junction causes a flow of electrons to the *n*-type side and holes to the *p*-type side of the junction.

1. c. Types of Solar Cells:

There are several kinds of solar cells that are currently available. However, each of them is based on different concepts and each has its unique advantages. Analysis and comparison between different cells (or technologies) will help us to adopt the most efficient and beneficial technology, given a specific set of conditions.

1. c. 1. Silicon cells:

Silicon or other semiconductor materials used for solar cells can be single crystalline, multi crystalline, polycrystalline or amorphous. The key difference between these materials is degree to which the semiconductor has a regular, perfectly ordered crystal structure, and therefore semiconductor material may be classified according to their size of the crystals.

Descriptor	Symbol	Grain Size	Common Growth Techniques
Single crystal	sc-Si	>10cm	Czochralski (CZ) float zone (FZ)
Multicrystalline	mc-Si	1mm-10cm	Cast, sheet, ribbon
Polycrystalline	pc-Si	1µm-1mm	Chemical-vapour deposition
Microcrystalline	µc-Si	<1µm	Plasma deposition

Figure 1.b: Difference in grain size and techniques for various types of silicon cells [4].

1. c. 1. 1. Single-crystalline silicon cells:

Single-crystalline wafers typically have better material parameters but they are more expensive. Crystalline silicon has an ordered crystal array, with each atom ideally lying in a pre-determined position. Crystalline silicon exhibits predictable and uniform behavior but because of the careful and slow manufacturing processes required, it is also the most expensive type of silicon.

1. c. 1. 2. Multi-crystalline silicon cells:

Techniques for the production of multicrystalline silicon are more simple and cheaper, than those required for single crystal material. Multicrystalline materials consists of grain boundaries and this is why the material quality is lower than that of single crystalline materials. Grain boundaries introduce high localized regions of recombination due to the introduction of extra defected energy levels into the band gap, thus reducing the overall minority carrier lifetime from the material. In addition, grain boundaries reduce the performance of the solar cell by blocking carrier flows and providing shunting paths for current flow across the *p-n* junction.

1. c. 2. Thin film solar cells:

Multiple compounds like CdS, CdTe, Cu(In,Ge)Se₂, GaAs etc. are used to fabricate thin filmsolar cells. One example of thin Film is a ZnO/CdS/CuInGaSe₂ thin-film solar cell. Conversion efficiencies exceeding 19% have been achieved here [5].

1. c. 3. Polymer solar cells:

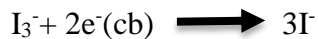
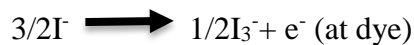
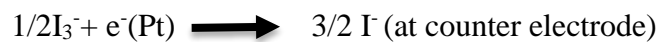
A polymer solar cell consists a conjugated polymer, with delocalized π electrons, which can absorb visible light and conduct electrical charge. For example, a low-band-gap alternating copolymer consisting of terthiophene and isoindigo has been designed and synthesized. Solar cells based on this polymer and PC₇₁BM ([6,6]-phenyl-C71-butyric acid methyl ester) show a power conversion efficiency of 6.3%, which is a record for polymer solar cells based on a polymer with an optical band gap lower than 1.5 eV [6].

1. c. 4. Dye Sensitized Solar Cell:

Dye-sensitized solar cells (DSSC) provide a credible alternative concept to present day $p-n$ junction photovoltaic devices with respect to the technical and economical view. Here, light is absorbed by the sensitizer, which is anchored to the surface of a semiconductor having wide band gap. Charge separation takes place at the interface via photo-induced electron injection from the dye to the conduction band (CB) of the solid. The carriers are transported in the CB of the semiconductor to the charge collector. Nearly quantitative conversion of incident photon into electric current is gained over a large spectral range from the UV to the near IR region. It is possible to produce these cells at a lower cost than other conventional devices.

The work on dye sensitized solar cells (or Gratzel cells) was first published in 1991. Highest Lab level efficiencies are more than 15%. They are cost effective compared to Si solar cells, easy to assemble and fairly stable [7].

In the figure below, the schematic of a DSSC is shown applied on a conductive FTO glass plate and the sensitizing dye (like Ru-dye) is deposited on the wide gap semiconductor. The electrolyte is a redox couple (usually iodide/tri-iodide) that is in contact with the dye and it reduces the oxidized dye and carries the positive hole to the counter electrode. The overall reactions are given below.



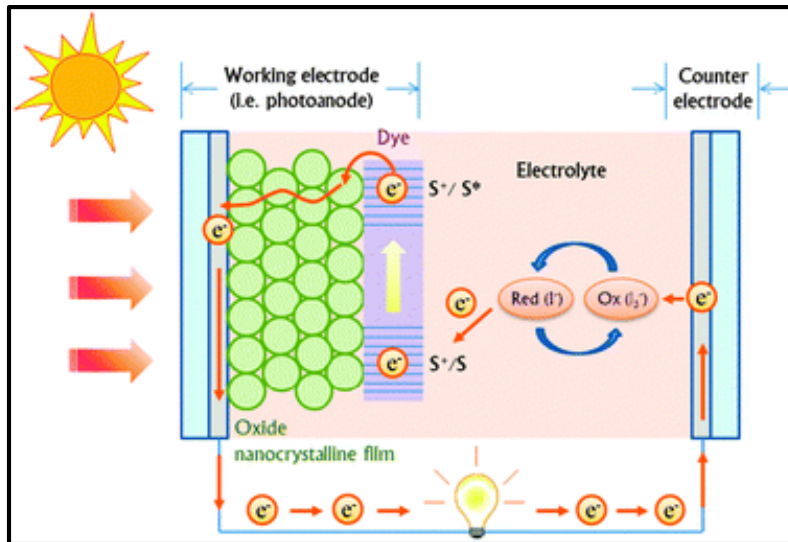


Figure 1.c: A schematic representation of dye working mechanism of a DSSC [8].

1. c. 2. a. Advantages:

- Dye-sensitized solar cells have a good depth in their nanostructure and hence absorb well the photons well in the sunlight. Furthermore the dyes used in the cells are efficient in converting the absorbed photons into electrons.
- As the manufacturing cost is reduced, DSSCs are less expensive when compared to other semiconductor cells.
- The dye used in dye-sensitized solar cells can absorb diffuse sunlight and fluorescent light as well. DSSCs can also work in cloudy weather and low-light conditions without much impact on efficiency, while other traditional cells would fail at illumination below a certain range.
- Unlike other thin-film cells, DSSCs do not degrade in sunlight over time which makes the cells last long.
- DSSCs are mechanically robust. They are made of lightweight materials and require no special protection from rains or trees or any other harsh objects [9].

1. c. 2. b. Disadvantages:

- The major disadvantage of a DSSC design is the use of the liquid electrolyte, which has temperature stability problems. At low temperatures the electrolyte can freeze, ending

power production and potentially leading to physical damage. Higher temperatures cause the liquid to expand, making sealing the panels a serious problem.

- Another disadvantage is that the costly ruthenium (dye), platinum (catalyst) and conducting glass or plastic (contact) are needed to produce a DSSC.
- A third major drawback is that the electrolyte solution contains volatile organic compounds (or VOCs), solvents which must be carefully sealed as they are hazardous to human health and the environment.
- Replacing the liquid electrolyte with a solid has been a major ongoing field of research. Recent experiments using solidified melted salts have shown some promise, but currently suffer from higher degradation during continued operation, and are not flexible.

1. c. 3. Quantum dot sensitized solar cells (QDSSCs):

The emergence of quantum dot-sensitized solar cells (QDSSCs) has provided an alternative way to harvest solar light for energy conversion [10]. Quantum dots are used as a photosensitized materials in QDSSCs. Quantum dots are tiny particles, have discrete energy levels and band gaps are tunable across a wide range of energy levels by changing the QD size in contrast to bulk materials, where the band gap is fixed.

1. c. 3. 1. Quantum Dots:

Quantum dots are tiny particles or nanocrystals of a semiconducting material with diameters in the range of 2-10 nanometers (10-50 atoms). Quantum dots display unique electronic properties, intermediate between those of bulk semiconductors and discrete molecules, that are partly the result of the high surface-to-volume ratios for these particles.

The discrete, quantized energy levels of quantum dots relate them more closely to atoms than that of bulk materials and this is why quantum dots are nicknamed as 'artificial atoms'. Quantum dots can be classified into mainly three types based on their composition and structure.

1. c. 3. 1. a. Core-Type Quantum Dots:

These type of QDs are mainly single component materials with uniform internal compositions, such as chalcogenides (selenides or sulfides) of metals like cadmium or zinc. Example: CdSe

1. c. 3. 1. b. Core-Shell Quantum Dots:

One QD embedded in another, with both comparative wide band gaps are known as core-shell quantum dots (CSQDs) or core-shell semiconducting nanocrystals (CSSNCs). For example, quantum dots with CdSe in the core and ZnS in the shell.

1. c. 3. 1. c. Alloyed Quantum Dots:

Multicomponent QDs offer an alternative method to tune properties without varying crystallite size. Alloyed semiconductor quantum dots with both homogeneous and gradient internal structures allow tuning of the optical and electronic properties by merely varying the composition and internal structure without changing the crystallite size. For example, alloyed QDs of the compositions $\text{CdS}_x\text{Se}_{1-x}/\text{ZnS}$ of particle size of 6 nm emits light of different wavelengths by just changing the composition.

1. c. 3. 2. Quantum confinement:

It describes how electronic properties (organization of energy levels into which electrons can climb or fall) and optical properties change when the semiconductor material size is in the range of 10 nm. Specifically, the phenomenon results from electrons and holes being squeezed into a dimension that approaches a critical quantum measurement, called the exciton Bohr radius.

Energy for the lowest excited state relative to E_{gap} is;

$$E_g^{\text{NC}} = E_g^{\text{B}} + (h^2\pi^2/2R^2)(1/m_e^* + 1/m_h^*) - 1.8e^2/\epsilon R$$

An analytical expression for how the electronic band gap of the semiconductor nanocrystal is modified relative to that bulk semiconductor. R is the *radius*, $m_{e,h}^*$ are the *effective masses* of electron and hole. 2nd term represents the confinement energy tends to increase the energy of the band gap as it scales with R^{-2} , 3rd term is a small Coulomb correction factor which accounts for the attraction between the e^- and the hole. In the bulk, the confinement energy term is absent so that the excitonic peak can be found below the band gap absorption [11].

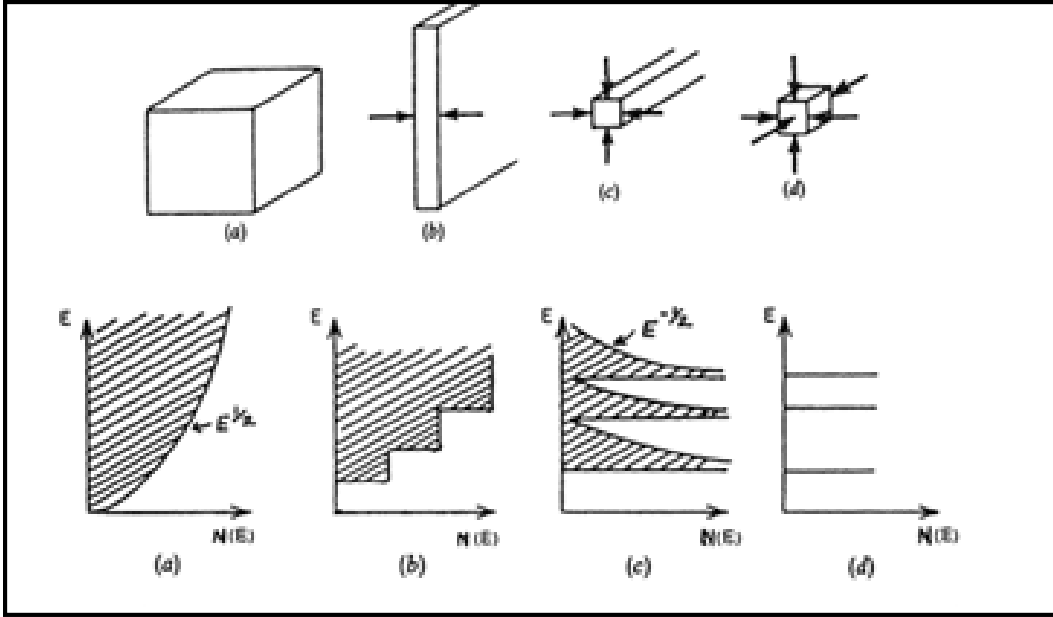


Figure 1.d: Density of states versus confinement. The electronic density of states for different dimensionalities of confinement: a) bulk; b) 1D confinement, 2D material; c) 2D confinement, 1D material; d) 3D confinement, 0D material [12].

1. c. 3. 3. Parameters of QDSSCs:

Here is some short discussion of parameters related to QDSSCs.

1. c. 3. 3. a. IV curve of a solar cell:

The IV curve of a solar cell is the superposition of the IV curve of the solar cell diode in the dark with the photo-generated current. The light has the power to shift the IV curve down into the fourth quadrant where power can be extracted from the diode. Illuminating a cell adds to the normal "dark" currents in the diode. So that the diode law becomes:

$$I = I_0 [\exp(qv/nkT)-1] - I_L$$

The equation for the IV curve in the 1st quadrant is:

$$I = I_L - I_0 [\exp(qv/nkT)-1]$$

The -1 term in the above equation is usually neglected and the exponential term is usually $\gg 1$ except for voltages below 100 mV. Further, at low voltages, the light generated current I_L dominates over the I_0 term so the -1 term is not needed under illumination.

1. c. 3. 3. b. Short-circuit current (I_{sc}):

The short-circuit current is the current through the solar cell when there is no voltage across the solar cell (i.e., when the solar cell is short circuited).

1. c. 3. 3. c. The open-circuit voltage (V_{oc}):

It is the maximum voltage available from a solar cell, and this occurs when the current is zero.

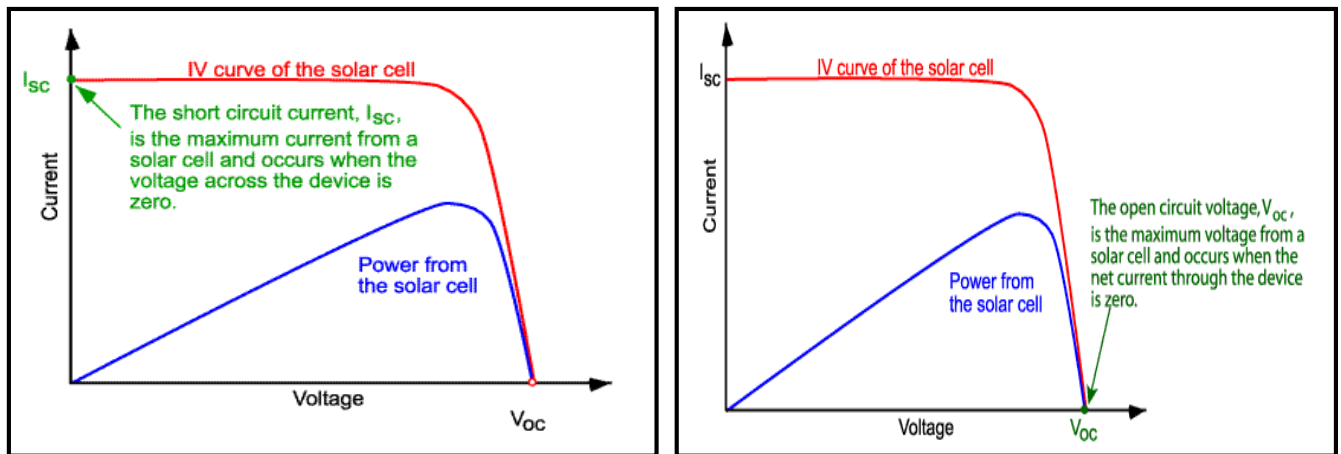


Figure 1.e: Representation of I_{sc} and V_{oc} in characteristic I - V curve.

1. c. 3. 3. d. Fill Factor:

The "fill factor", more commonly known by its abbreviation "FF", is a parameter which, in conjunction with V_{oc} and I_{sc} , determines the maximum power achieved from a solar cell.

$$FF = \frac{I_{max} \times V_{max}}{I_{sc} \times V_{oc}} \quad (1)$$

1. c. 3. 3. e. Efficiency:

It is the most commonly used parameter in a solar cell to compare the performance of one solar cell in that of another. Efficiency is defined as the ratio of energy output from the solar cell to input energy from sunlight.

$$\eta = \frac{V_{oc} J_{sc} FF}{P_{in}} \quad (2)$$

Where in the above equation, P_{in} is the input power, and the input power for efficiency calculations is 1 kW/m^2 or 100 mW/cm^2 . Thus the input power for a $100 \times 100 \text{ mm}^2$ cell is 10 W and for a $156 \times 156 \text{ mm}^2$ cell, it is 24.3 W .

1. c. 3. 4. Working mechanism of QDSSCs:

The working mechanism of the QDSSC is as follows. At first the QDs absorb energy in terms of incident photon from sunlight and due to this the electrons are excited from the valence band of the QDs to the conduction band of the QDs. The excited electrons will be transferred to the conduction band of the wide band gap semiconductor (TiO_2) attached to the FTO glass and a hole is created in the valence band of the QDs. These holes are trapped by the redox couple of the electrolyte (sulfide or polysulfide). As a consequence, the electrolyte is reduced at the counter electrode and it moves to the anode and regenerates the QDs.

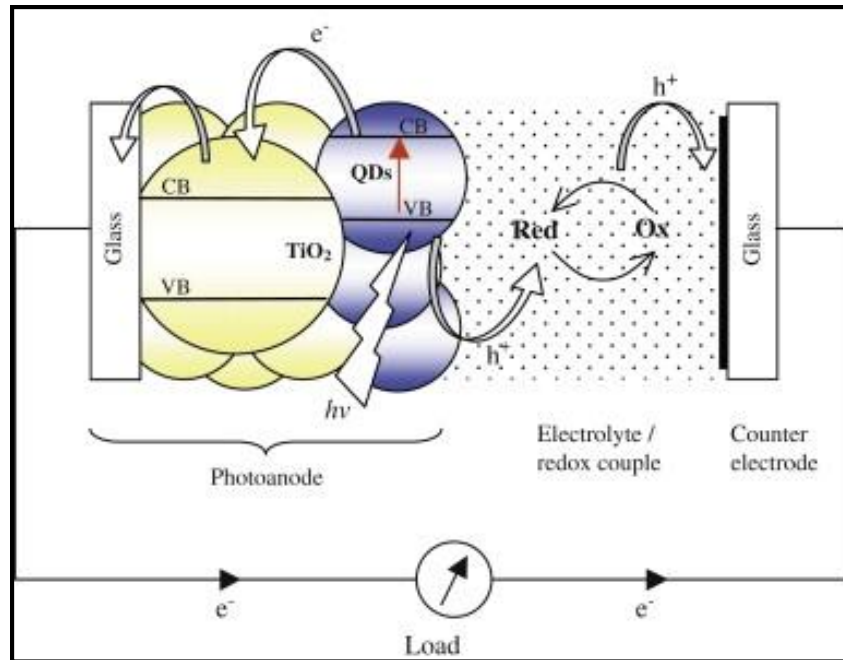


Figure 1.f: Schematic representation of working mechanism of QDSSC [13].

1. c. 3. 5. Advantages over DSSCs:

- QDSSCs have a special property of tunability of optical properties with size.
- Most of the dyes are more susceptible to U.V. degradation, but QDs are not.
- QDSSCs form better hetero-junctions with solid hole conductors in comparison with DSSCs.
- Higher intrinsic dipole moment of QDs may lead to rapid charge separation and band alignment.

1. c. 3. 6. Deposition of semiconductor QDs over mesoscopic TiO₂ films:

Quantum Dots are developed over a wide gap semiconductor (TiO₂) through mainly in two approaches, post synthesis assembly, and direct growth. In the first method, pre-synthesized quantum dots (QDs) are bound to TiO₂ where organic molecules acts as a linkers. The latter method (direct growth) includes SILAR (Successive Ionic Layer Absorption and Reaction), CBD (Chemical Bath Deposition), Electrophoretic Deposition (EPD), Drop cast and spin coating etc. [14].

Deposition of QDs over mesoporous metal oxides is focused on mainly two approaches:

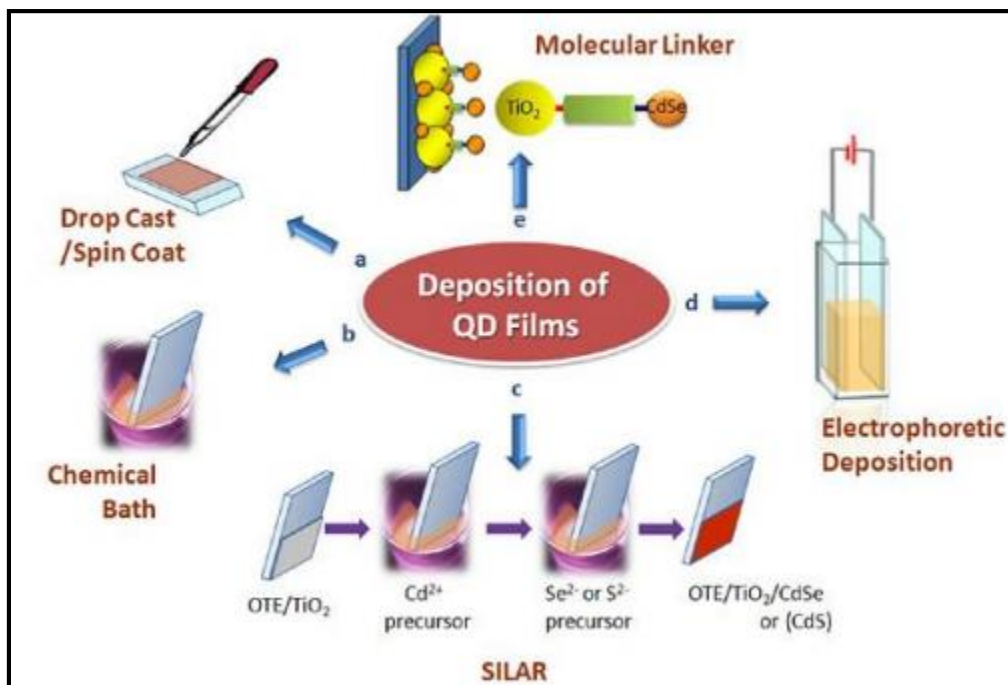


Figure 1.g: Representation of different methods of QD deposition [15].

- 1) Colloidal QDs are attached to the surfaces of metal oxides either by linker assisted method or other attractive forces through surface ligands.
- 2) QDs are deposited directly over TiO_2 anodes in CBD process under normal or hydrothermal conditions.

In a CBD process, cationic and anionic precursors are dissolved in either one bath or in two separated beakers and the bare electrode dipped alternatively in each other. The cationic and anionic precursors are reacted slowly to grow the QDs. Another one is the SILAR process which has been used to prepare various inorganic-semiconductor-modified electrodes. Mainly this process is followed for metal sulfides, but not of metal selenides or tellurides because of difficulties in preparing stable Se^{2-} and Te^{2-} precursors [16].

A maximum photo conversion efficiency of 3.67% was achieved for this CdS-sensitized TiO_2 electrode under a visible light illumination of 100 mW cm^{-2} using Pt as a counter electrode [17].

1. c. 3. 7. Recent trends of CdSeTe based on QDSSCs:

To increase the capable of arising solar cell efficiency, alloyed semiconductor quantum dots can be used near-IR region. CdSeTe (or $\text{CdSe}_x\text{Te}_{1-x}$), the ternary alloy, has the capacity to deliver high efficiencies.

CdSeTe is used in developing near-infrared fluorescent probes for in vivo molecular imaging and biomarker detection as it shows change in optical properties without changing the particle size [18].

In another work, CdSeTe QDs were deposited over TiO_2 and TiO_2/CdS films with a coating of ZnS by using various counter electrode like Pt nanoparticles, Cu_2S , Au, carbon nanomaterials and electrolytes iodide/tri iodide electrolytes (I^-/I_3^-), polysulfide electrolytes ($\text{S}^{2-}/\text{S}_x^{2-}$), and cobalt redox couples ($[\text{Co}(\text{o-phen})_3^{2+/3+}]$) to get 50% IPCE over 400-710 nm wavelength region [19].

$\text{CdSe}_{0.45}\text{Te}_{0.55}$ alloyed quantum dots (QDs) with an excitonic absorption at 800 nm and particle size of 5.2 nm were prepared via a non injection high-temperature pyrolysis route which gave a record conversion efficiency of 6.36% ($J_{\text{sc}}= 19.35 \text{ mA/cm}^2$, $V_{\text{oc}}= 0.571 \text{ V}$, $\text{FF} = 0.575$) under full 1 sun illumination with Cu_2S counter electrode and polysulfide as electrolyte.

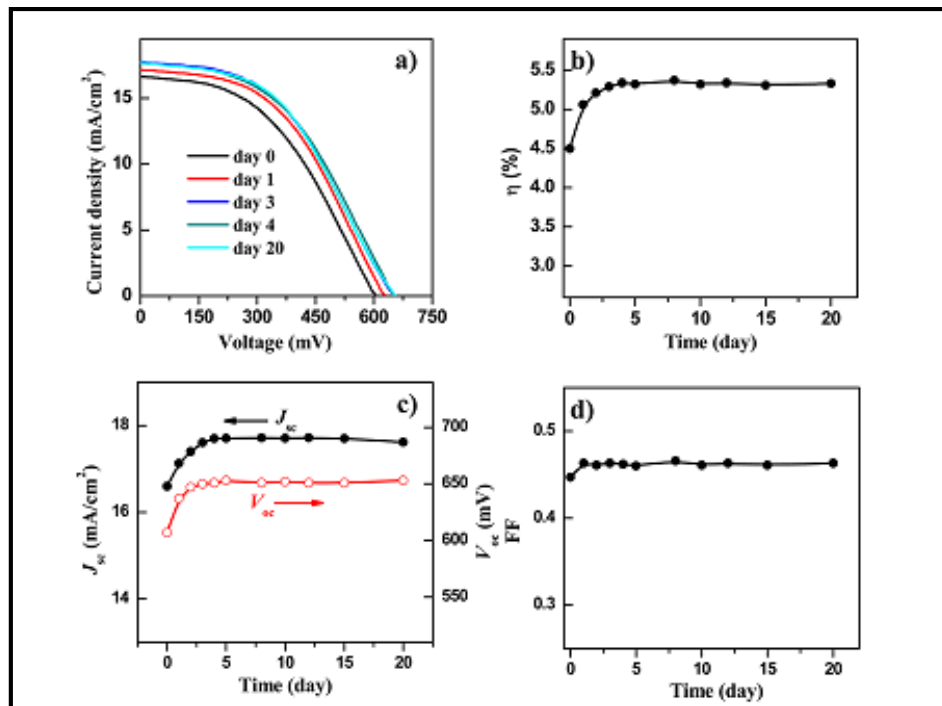


Figure 1.h: Temporal evolution of J-V curves (a) and photovoltaic parameter values, η (b), J_{sc} , V_{oc} (c), and FF (d), for the CdSeTe₈₀₀ cells based on Cu₂S counter electrodes via electrode position of Cu on FTO glass [20].

In new of the above described advantages CdSeTe QDs, in this thesis, CdSeTe based solar cells were developed with Reduced graphene oxide as the counter electrode.

2. Experimental details:

2. 1. Chemicals:

Degussa TiO₂ P25 (with surface area 50±15 m²g⁻¹) was a gift from Evonik; Titanium Chloride (TiCl₄), Triton X-100, Cadmium Acetate [Cd(CH₃COO)₂], Sodium sulfide (Na₂S), Zinc acetate dihydrate ultrapure[(CH₃COO)₂Zn.2H₂O] were purchased from Merck; Acetyl acetone, Graphite powder (<20µm), Cadmium oxide (CdO), Trioctylphosphine(TOP) from Sigma Aldrich. Ultrapure water with a resistivity of ~18.2 MΩ cm was obtained through Millipore Direct-Q 3 UV system. Hydrogen peroxide (H₂O₂, 30 wt %), Potassium permanganate (KMnO₄), methanol, ethanol, Acetyl nitrile, toluene, Sulfuric acid (95 %), Hydrochloric acid, Hydrogen monohydrate, Paraffin heavy, Oleic acid, Starch soluble GR, n-hexane were obtained from Merck. Selenium powder (99+ %), Tellurium powder (-200mesh, 99.5 % metal basis gray powder) were obtained from Alfa Aesar. Inorganic transparent electrodes of SnO₂:F coated glass (FTO, Pilkington, sheet resistance: 25 Ω/sq) were cleaned in a soap solution, Ethanol, double distilled water, propan-2-ol and acetone prior to use.

2. 1. 1. Preparation of CdSe_xTe_{1-x}:

Here a literature method was followed with minor modification. Typically, 0.5 mL of 0.1 M Se and Te precursor solutions, prepared by dissolving Se or Te in TOP and paraffin (v/v, 1:3) at 60 or 250 °C under N₂ atmosphere, respectively. Both of the precursors were mixed with 10 mL of 0.1 M Cd (50 mg) stock solution (when it became colorless), obtained by dissolving CdO in oleic acid (460 mg); TOP and paraffin and (v/v, 1:2) at 200 °C under N₂ in a three-neck flask clamped in a heating mantle with a Cd:Te:Se molar ratio of 10:1:1. Afterwards, the resulting reaction mixture was further heated to 320 °C at a rate of 10 °C/min under a N₂ atmosphere with vigorous stirring. After maintaing at 320 °C for 15 min the reaction mixture was removed from the heater

and cooling to 60 °C. Then 30.0 mL of hexane-methanol (v/v, 1:1) was used as the extraction solvent to separate the nanocrystals from by products and unreacted precursors, if present. The prepared CdSe_xTe_{1-x} QD solution was further purified by centrifugation and decantation with the addition of acetone. The prepared QD solution was used in toluene solvent after washing it by acetonitrile and toluene [20].

2. 1. 2. Preparation of Carbon Nanospheres:

Starch, the carbon source, was dissolved in 6 M sulfuric acid (16.3 mL of 18.4 M was taken to form 50mL 6 M acid solution) to form a starch solution, which was placed in a round bottom flask and refluxed at 120 °C for 12 h. The resulting black suspension was filtered and washed by distilled water. Next the product was dried overnight and annealed at 350 °C for 3 h. [21].

2. 2. Preparation and reduction of Graphite Oxide (GO):

Graphite powder (200 mg) was mixed with 5 mL of H₂SO₄ (95%) and the mixture was stirred for 30 min by maintaining the temperature at 20 °C. Potassium permanganate (600 mg) was added very slowly in the suspension with vigorous stirring while maintaining a reaction temperature of 20 °C. Then the ice bath was removed, and there action mixture was stirred overnight at 35 °C. In the next step water was added to the pasty solution with constant agitation and the color of the solution changed to yellowish brown .After 2 h of vigorous stirring, 5 mL of 30% H₂O₂ was added to the yellowish brown solution and immediately it turned to golden yellow. The mixture was washed with 5% HCl and then deionized water to make the solution became acid free. Then the mixture was filtered and dried under vacuum at 65 °C. The GO was obtained as a gray powder. In order to prepare reduced GO, 0.1 g of GO was dissolved in 50 mL of deionized water. Then 1 mL of hydrazine monohydrate was added to the reaction mixture and heated up to 95 °C for 12 h. The reduced graphite oxide was collected by filtration as a black powder. The product thus obtained was washed with deionized water to remove excess hydrazine, and the final product was dried in a vacuum oven at 75 °C for one day [22].

2. 3. Fabrication of Photoanode:

A dense TiO₂ layer was laid over FTO using a paste of TiO₂ powder dispersed uniformly in a clear formulation of acetyl acetone (1.5 mL), ultrapure water (8.5 mL) and Triton X-100 (20 mg) by

doctor blading. The as-deposited TiO₂ plates were heated at 58 °C for 30 min, which was followed by annealing at 500 °C for another 30 min. Again one more layer of TiO₂ was also deposited using the same steps as mentioned above, followed by heating and annealing as performed for the active layer. Then the TiO₂ layered FTO substrates were kept immersed in an aqueous TiCl₄ (0.04 M) solution at 70 °C for 20 min and the resulting TiO₂ film was rinsed in distilled water and sintered at 500 °C [23].

A CdS layer was deposited over the TiO₂ plates by Successive Ionic Layer Absorption and Reaction (SILAR) process by immersing a FTO/TiO₂ in a 0.1(M) methanolic solution of Cd(OAc)₂ and Na₂S for 2 min followed by a methanol rinse and dried. In case of TiO₂/CNS/CdS was prepared by using very dilute solution of carbon nanospheres in ethanol over TiO₂ plates by electrophoretic deposition, then CdS layer was formed by usual SILAR process. CdSeTe quantum dot was deposited over TiO₂ or CdS through electrophoretic deposition at high voltage. In case of CdSeTe QDs ZnS layer was grown over CdSeTe through SILAR process thus it can make shield on excess Cd (Cd:Se:Te = 10:1:1 in CdSe_xTe_{1-x}).

2. 4. Fabrication of Counter Electrode:

The newly formed reduced graphene oxide was annealed at 350 °C for 3.5 hours and it was deposited over FTO plates at 60V for 10 minutes in Ethanol solution. Then the FTO plates with a RGO layer were annealed at 140 °C for another 10 minutes. Now these plates were used as a counter electrode in this QDSSCs.

2. 5. Electrolyte:

All experiments were performed using a 0.1 M Na₂S in ultrapure water/methanol 3:7 (v/v) solution employed as the electrolyte.

3. Results and discussion:

3. 1. UV-Vis spectroscopy analysis:

Ultraviolet/Visible (UV/Vis) spectroscopy is a technique used to quantify the light that is absorbed and scattered by the sample. The sample is placed between a light source and a photodetector, and the intensity of a beam of light is measured before and after passing through the sample. These measurements are compared at each wavelength to quantify the sample's wavelength dependent extinction spectrum. The data is plotted typically a function of wavelength.

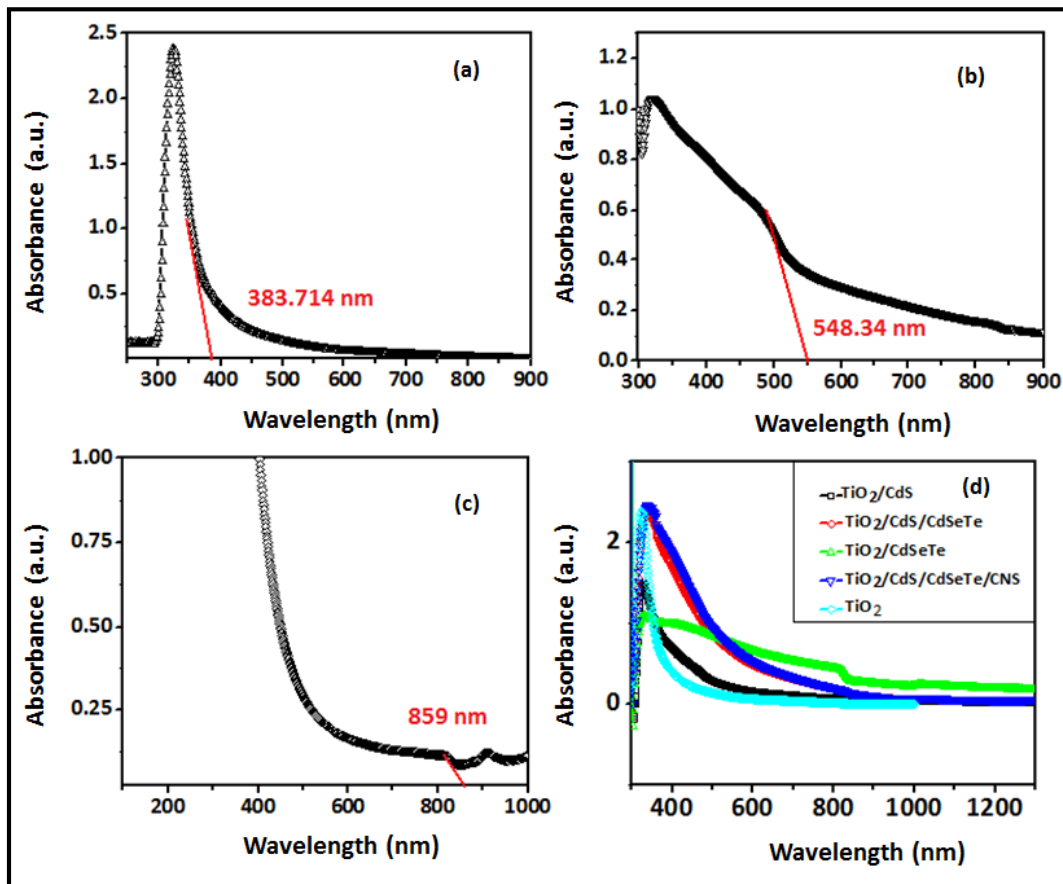


Figure 3.a: UV-Vis spectral analysis of (a) TiO₂, (b) CdS, (c) CdSeTe and (d) all the photoanode films used in QDSSCs.

From the above absorption spectrum it is observed that TiO₂, CdS, CdSeTe show absorption peaks at 383 nm, 548 nm and 859 nm respectively. The optical band gap is easily calculated by using the formula: Band gap (eV) = $[1240/\lambda \text{ (nm)}]$.

Using the above formula the calculated optical band gaps of TiO₂, CdS and CdSeTe are 3.23, 2.26 and 1.44 eV respectively.

3. 2. Cyclic Voltammetric analysis:

A typical cyclic voltammogram is recorded for a reversible single electrode transfer reaction.

CV is a cyclic diagram, voltage vs current plot from which the conduction band and valence bands are determined.

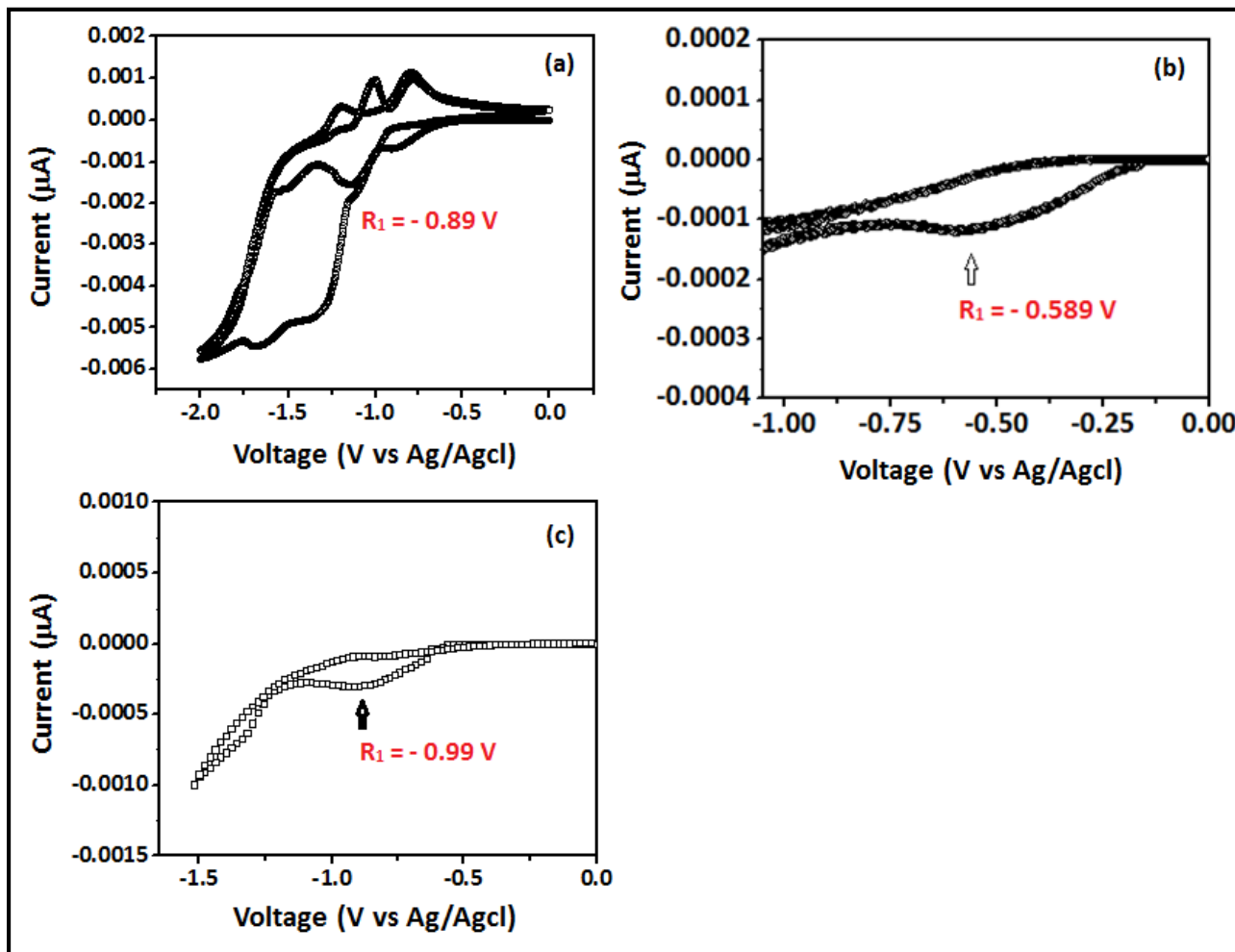


Figure 3.b: Cyclic voltammograms of (a) CdS, (b) TiO₂ and (c) CdSeTe.

Cyclic voltammograms were recorded at a scan rate of 20 mV s^{-1} in a 0.1 M NaOH solution in three electrode electrochemical cells with (a) CdS/FTO, (b) TiO₂/FTO and (c) CdSeTe/FTO as working electrodes in each case, Ag/AgCl/KCl as reference electrode.

The cyclic voltammograms of CdS, TiO₂ and CdSeTe show the first reduction peak (labeled as R₁ for each electrode in Figure 3.b) at, -0.89, -0.589 and -0.99 V (versus Ag/Ag⁺) in their cathodic branches respectively. The potential of reference electrode (Ag/Ag⁺) was +0.197 V (versus NHE). The reduction potential (versus NHE) corresponds to the LUMO of the electroactive material.

Therefore, the reduction potential of TiO₂ (versus NHE) will be: $E_R = (-0.589 + 0.197) \text{ V} = -0.392 \text{ V}$. Similarly, the reduction potential of CdS (versus NHE) will be: $E_R = (-0.89 + 0.197) \text{ V} = -0.693 \text{ V}$ and that of CdSeTe (versus NHE) will be: $E_R = (-0.99 + 0.197) \text{ V} = -0.793 \text{ V}$. A potential of 0 V (versus NHE) corresponds to 4.5 eV (w.r.t. vacuum level). The LUMO or CB positions of TiO₂, CdS and CdSeTe were therefore calculated to be 4.1, 3.8 and 3.7 eV and these values were used in the energy band diagram shown in Figure 3.p.

From the UV-Visible spectrum analysis we had calculated the corresponding band gaps and by combing this data with the CBs obtained from CVs, the calculated HOMO or VB positions of TiO₂, CdS and CdSeTe were 7.33, 6.06 and 5.14 eV.

3. 3. XRD analysis:

X-ray diffraction is used in two main areas: for the fingerprint characterization of crystalline materials and to determine their structures. Each crystalline solid has it's unique characteristic X-ray powder pattern which is used as a "fingerprint" for its identification. Once the material has been identified, X-ray crystallography may be used to determine its structure, i.e. determination of the size and the shape of the unit cell.

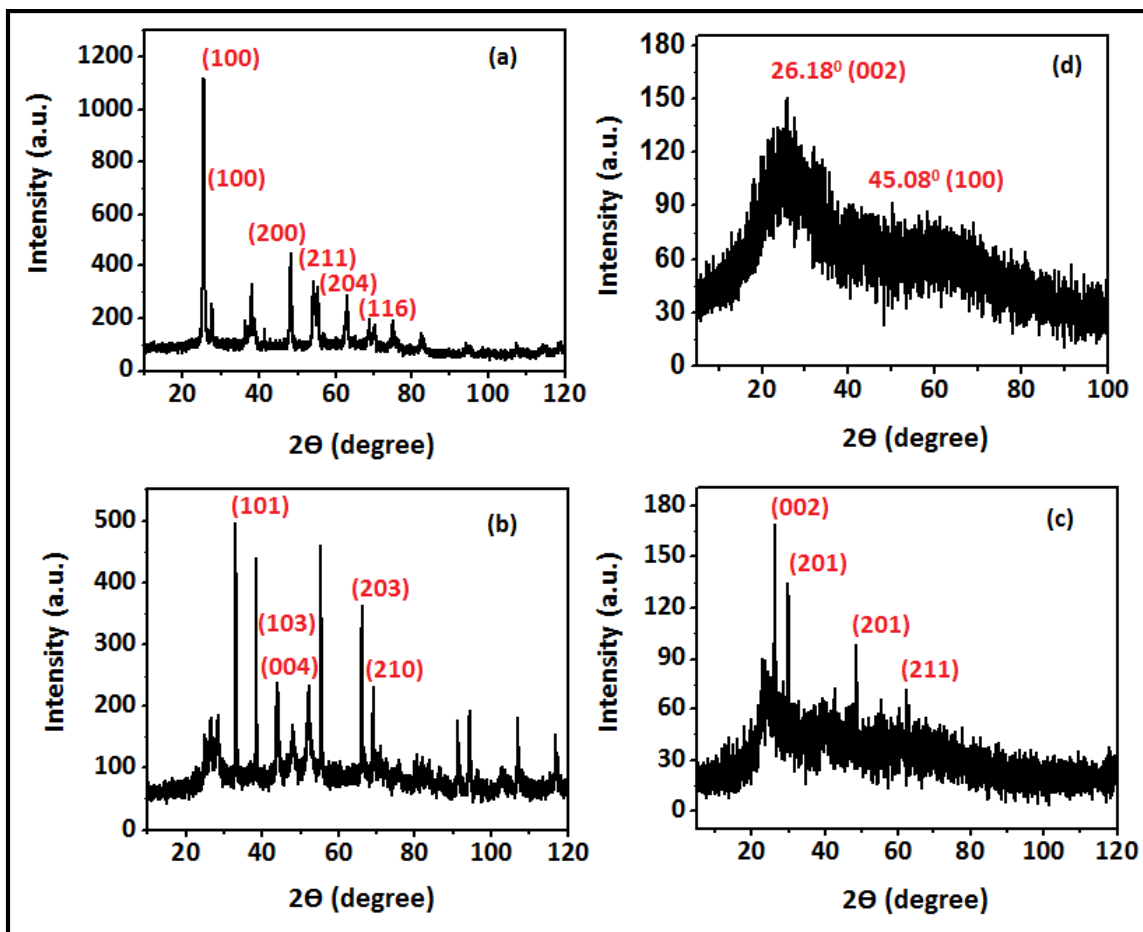


Figure 3.c: XRD patterns of (a) a TiO₂ film, (b) a CdS QDs film, (c) a CdSeTe QDs film and (d) a carbon nanospheres all on glass.

X-ray diffractograms of a TiO₂ film and films of CdS and CdSeTe QDs grown by SILAR separately on glass substrates are shown in Figure 3.c. The XRD pattern of TiO₂ shows peaks at $d = 3.51, 3.24, 1.89, 1.69, 1.47, 1.34 \text{ \AA}$, which concur well with the (100), (100), (200), (211), (204), and (116) planes of the body-centered tetragonal crystal structure of TiO₂, respectively, as per the PDF number 894921. The XRD pattern of CdS QDs shows broad peaks at $d = 3.42, 2.97, 2.1, 1.79 \text{ \AA}$, which can be attributed to the (101), (103), (004), and (203) planes of the face-centered cubic or fcc lattice of CdS (PDF: 652887). CdSeTe QDs produced d lines at $2.94, 1.87, 1.66, 0.954 \text{ \AA}$, which have been assigned to (002), (201), (201), (211) planes of CdSeTe with a fcc lattice (PDF: 411325).

An X-ray diffraction study of Carbon Nanospheres (CNS) has been done and by comparing with previous literature data the (hkl) planes are assigned. The XRD pattern of CNS shows peaks at $2\theta = 26.18^\circ, 45.085^\circ$ which concur well with the (002), (100) planes [24] of graphite.

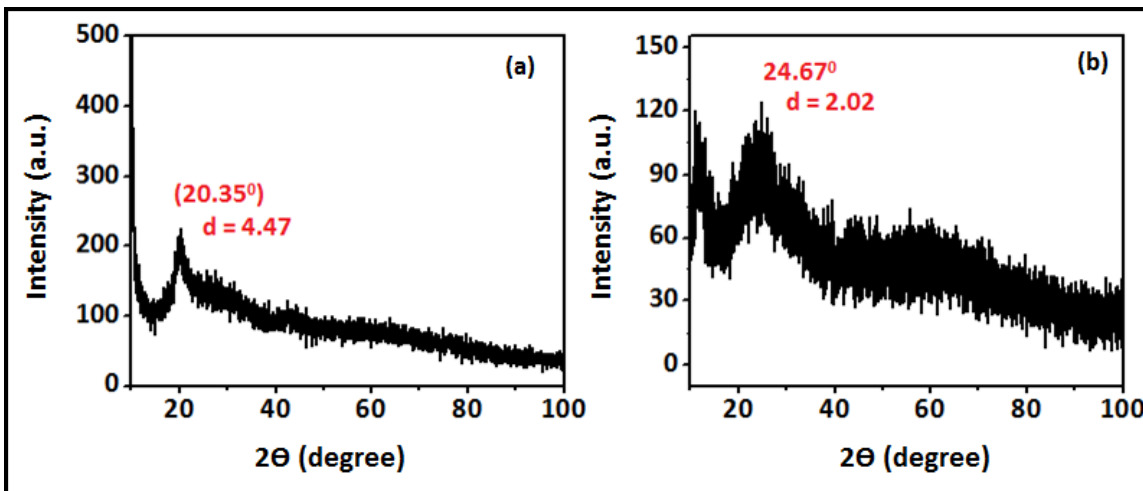


Figure 3.d. XRD patterns of (a) Graphene oxide (GO) and (b) Reduced graphene oxide (RGO).

X-ray diffractograms of Graphene oxide shows peak at $d = 4.47$ Å which can be attributed to the $2\theta = 20.35^\circ$. Similarly the XRD pattern of RGO shows a peak at $d = 2.02$ Å assigned to $2\theta = 24.67^\circ$.

3. 4. SEM analysis:

The scanning electron microscope (SEM) uses a focused beam of high-energy electrons to generate images of surfaces of solid samples.

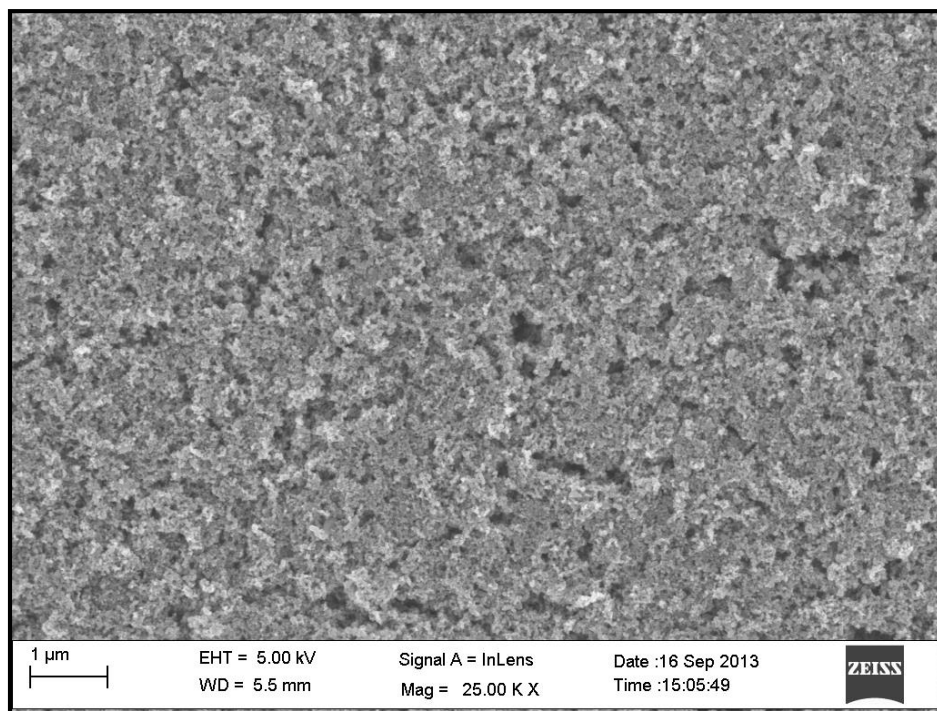
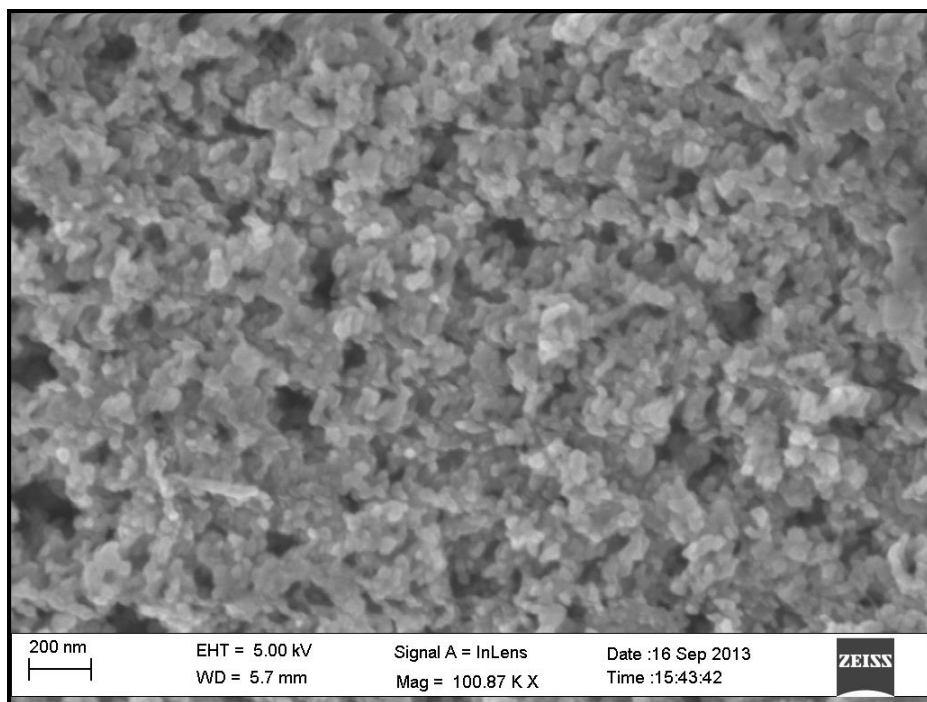


Figure 3.e: SEM images of TiO₂. A TiO₂ films have a granular porous morphology with pore sizes in the range of 25-175 nm. Such a porous structure is most advantageous for anchoring CdS and CdSeTe QDs through SILAR across the cross-section of TiO₂.

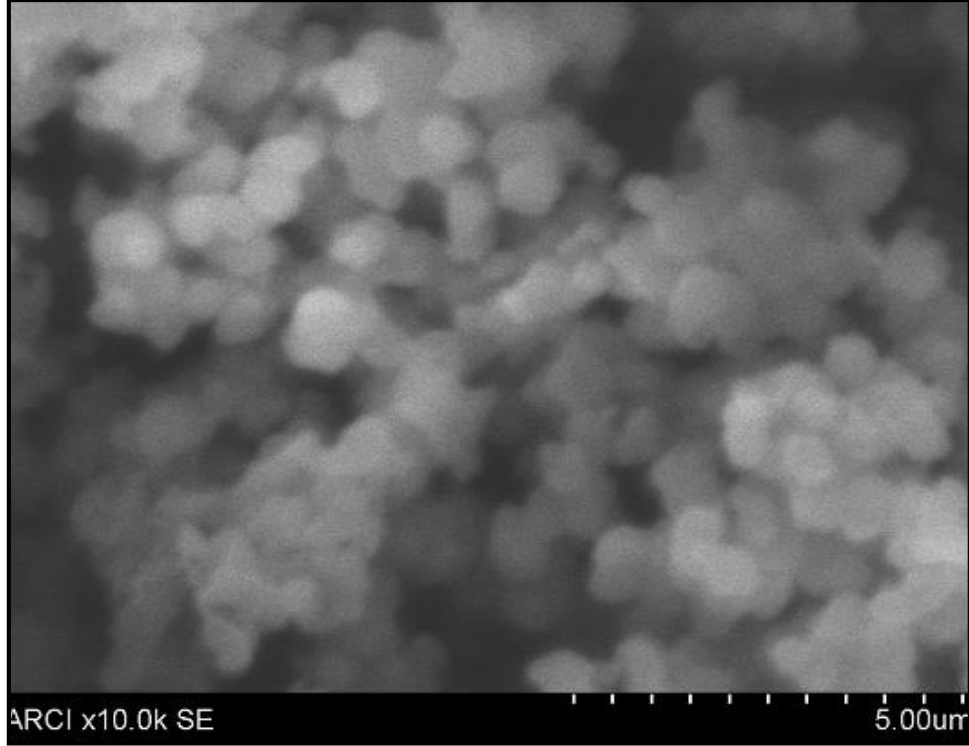


Figure 3.f: SEM image of Carbon Nanospheres with pore sizes in the range of 200-250 nm.

3. 5. Determination of equilibrated Fermi level of Carbon Nanospheres:

In KPFM (Kelvin probe force microscopy), an ac bias is applied to a conducting Pt/Ir tip of a known work function, it scans the sample surface and the localized contact potential difference (V_{CPD}) that arises between the conducting tip and the sample surface, is used for generating the surface potential map, as shown in the following equation.

$$V_{CPD} = (\Phi_{tip} - \Phi_{sample}) / e^- \quad (1)$$

Φ_{tip} is the work function of the conducting Pt/Ir coated Si cantilever (5.5 eV) and Φ_{sample} is the work function of the sample, i.e. the CNS/FTO electrode, which can be approximated to its' Fermi level position. The work function of Pt/Ir tip was first calibrated with highly ordered pyrolytic graphite (HOPG) ($\Phi_{HOPG} = 4.6$ eV) to convert the measured V_{CPD} to absolute surface work function. The absolute surface work function of the sample was calculated with equation (2).

$$\Phi_{sample} = 4.6 \text{ eV} + V_{CPDHOPG} - V_{CPDsample} \quad (2)$$

In KPFM, the topography of the film surface is measured in tapping mode and the surface potential variation is measured with conducting tip. The tip was held at ~ 100 nm above the film surface, and it is charged due to the applied ac potential. The sample surface is also charged since it is in the vicinity of the charged tip. The surface potential of the CNS/FTO assembly was 65 mV and the corresponding work function calculated using equation (2) was 4.55 eV. KPFM was performed on the electrode using a Veeco, Multimode 8 with ScanAsyst (Nanoscope 8.10 software) microscope. The sample deposited on FTO coated glass was affixed on a stainless steel disk with a conducting carbon tape. A thin strip of pin-hole free silver paste was used for taking contacts. The equilibrated Fermi level position of the photoanode is 4.55 eV, which was used in Figure 3.p.

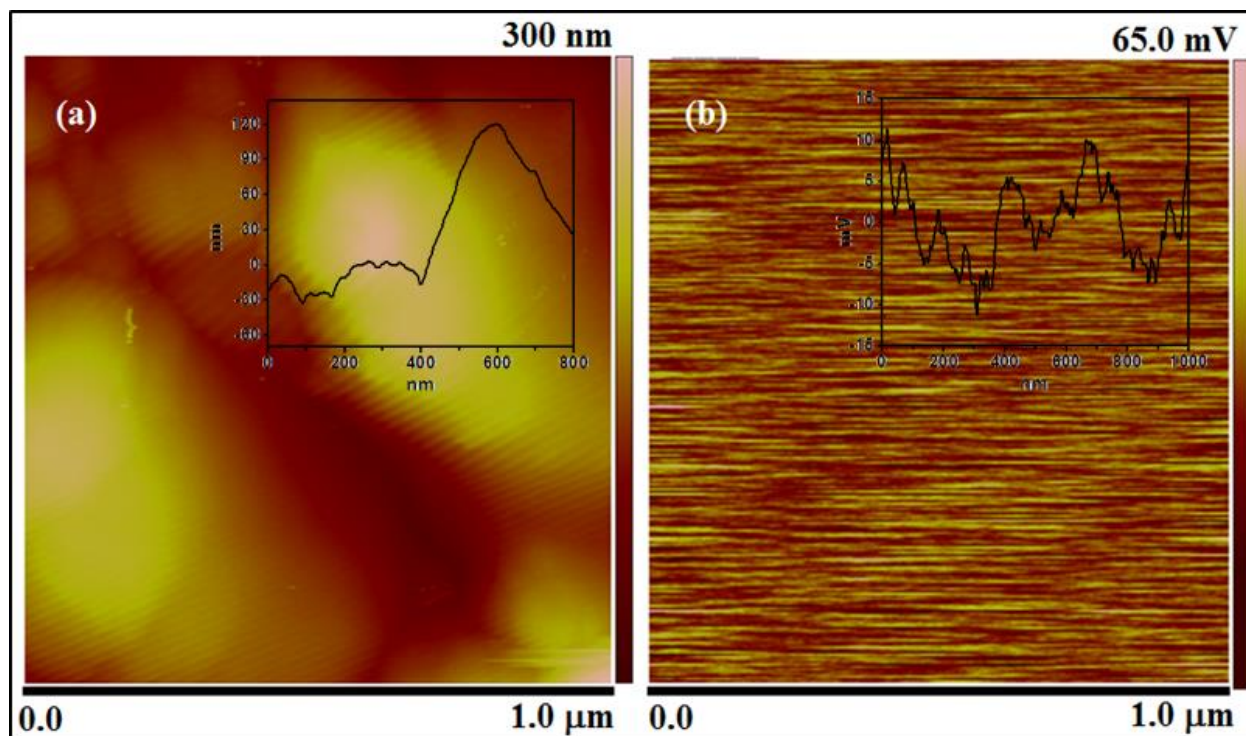


Figure 3.g: (a) Topography and (b) surface potential maps of the CNS/FTO electrode.

3. 6. Determination of conductivity by Linear Sweep Voltammetry analysis:

In linear sweep voltammetry (LSV) a fixed potential range is employed much like potential step measurements.

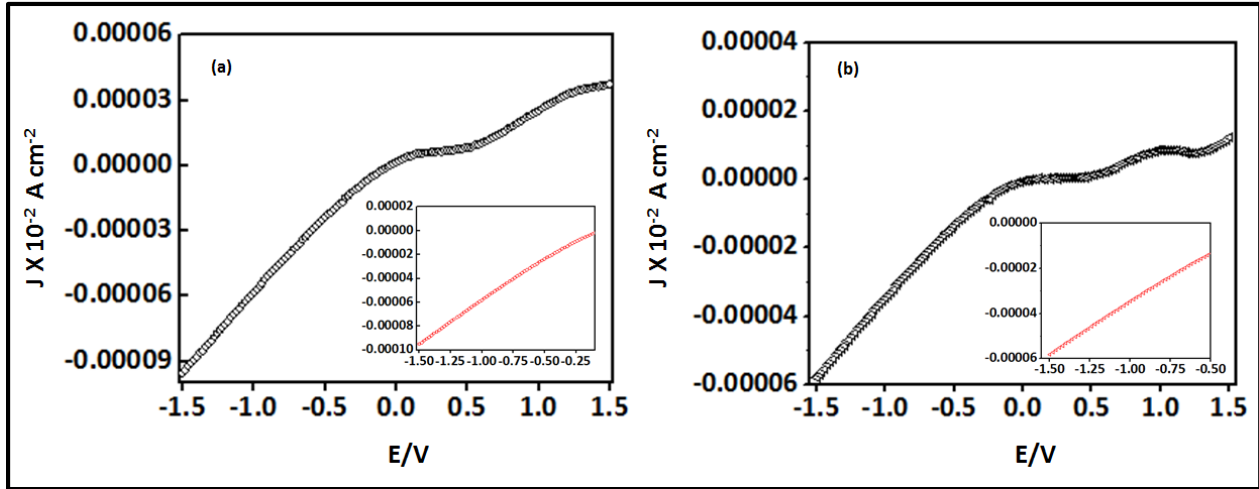


Figure 3.h: Linear sweep voltammograms of (a) Carbon Nanospheres and (b) Reduced graphene oxide; linear part of the each plot is shown in the insets from where the slope were calculated.

From figure 3.h (a) the average conductivity (σ) of Carbon Nanospheres was deduced from the slopes, using the eqn. $\sigma(\text{S cm}^{-1}) = J/V$ (slope, $\text{A cm}^{-2} \text{V}^{-1}) \times d$ (distance between the electrodes, cm). The conductivity was deduced to be **10.365 S cm⁻¹**. A linear part of the same plot is shown in the inset from where the slope is determined. The J–V dependence of CNS was non-linear in the -1.5 to +1.5 V range.

Similarly from figure 3.h (b) The average conductivity of Reduced graphene oxide was deduced from the slope was deduced to be **6.69 S cm⁻¹**. The J–V dependence of RGO was non-linear in the -1.5 to +1.5 V range.

3. 7. Mott-Schottky analysis:

The Mott–Schottky equation can be used to determine the flat-band potential of the semiconductor materials. It's derivation is essential for this experiment because it reinforces many key concepts associated with the semiconductor–electrolyte interface. However, in short, the starting point for the derivation is Poisson's equation in one dimension that describes the relationship between charge density and potential difference, ϕ , in a phase,

$$d^2 \varphi / dx^2 = - \rho / \varepsilon \varepsilon_0 \quad (1)$$

where ρ corresponds to the charge density at a position x away from the semiconductor surface and $\varepsilon, \varepsilon_0$ are the dielectric constant of the semiconductor and permittivity of free space respectively. Poisson's equation can be solved to give the Mott–Schottky equation:

$$\frac{1}{C^2} = \frac{2}{\varepsilon \varepsilon_0 A^2 e N_D} \left(V - V_{fb} - \frac{k_B T}{e} \right) \quad (2)$$

Here C and A are the interfacial capacitance and area, respectively, N_D is the number of donors, V is the applied voltage, k_B is the Boltzmann's constant, T is the absolute temperature, and e is the electronic charge. Therefore, a plot of $1/C^2$ against V should yield a straight line from which V_{fb} can be determined from the intercept on the V axis. The value of N_D can also be conveniently found from the slope knowing ε and A .

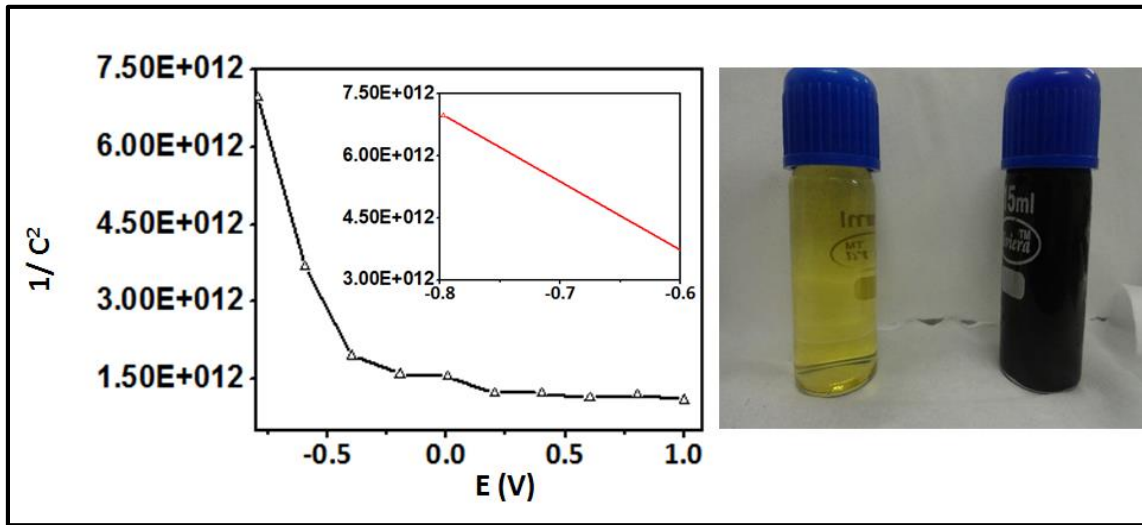


Figure 3.i: Mott Schottky diagram (linear part is in inset) of Carbon Nanosphere and the image of CNS in acid solution filtrate after washing (left) before washing (right).

In the inset the linear part of Mott Schottky plot is shown. From the line two points are assigned and slope is calculated which is 8.77. The slope with negative value represents that the Carbon Nanospheres is *p type*.

3. 8. FTIR spectroscopic analysis of RGO:

FT-IR stands for Fourier Transform Infrared, preferred method of infrared spectroscopy. In infrared spectroscopy and IR radiation is passed through a sample and as a result some of the infrared radiation is absorbed by the sample and some of it is passed through. The resulting spectrum represents the molecular absorption and transmission, creating a molecular “fingerprint” of the corresponding sample.

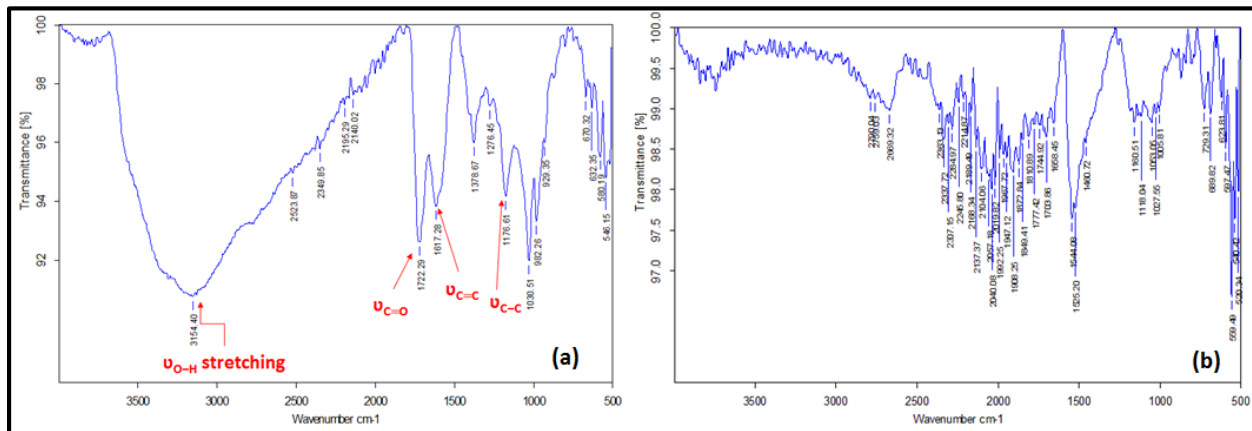


Figure 3.j: FTIR spectra of (a) GO and (b) RGO.

The FTIR peaks corresponding to the oxygen functionalities of GO were observed, and the assignments are presented below.

Data analysis:

3154 cm ⁻¹	O-H str. (H-bonding)
1722cm ⁻¹	Carbonyl (C=O) Carboxylic acid group
1630 cm ⁻¹	Ether or primary alcohol
1617 cm ⁻¹	C=C stretching
1176 cm ⁻¹	C-C stretching

3. 9. Raman spectroscopy analysis of GO and RGO:

Raman spectroscopy is a vibrational technique that is extremely sensitive to geometric structure and bonding within molecules and this sensitivity to geometric structure is extremely useful for the study of the different allotropes of carbon.

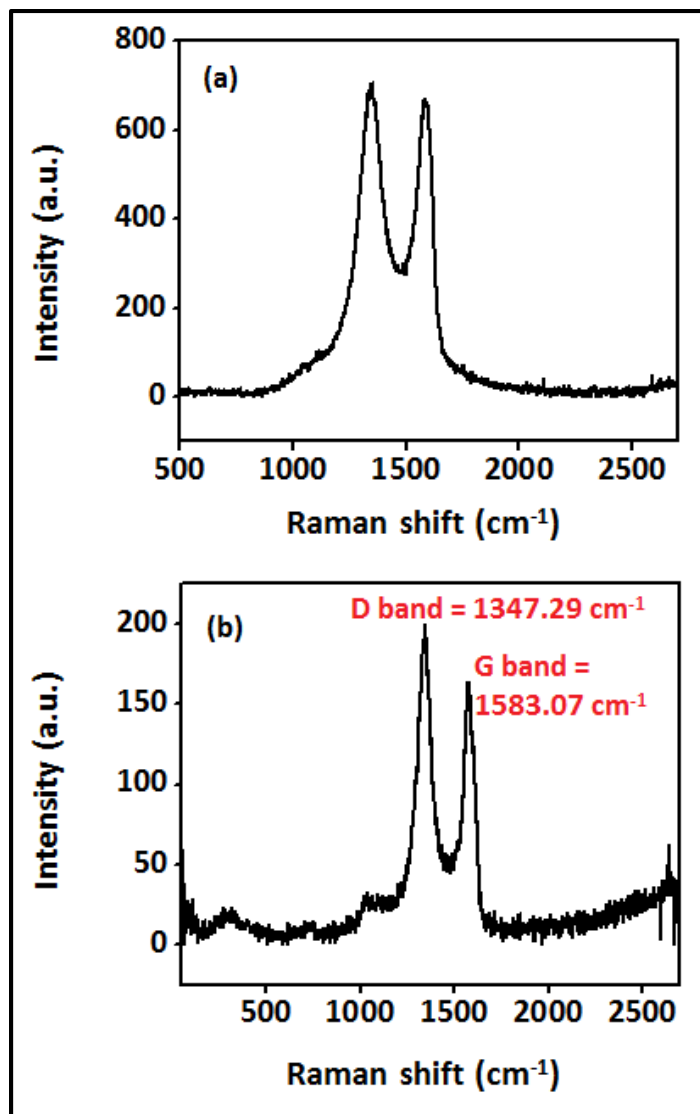


Figure 3.k: Raman spectra of (a) GO and (b) RGO.

The above figure shows the Raman spectra of Graphene oxide and Reduced graphene oxide. The D-band and G-band in RGO and GO are typically observed at 1347.29, 1583.07 cm^{-1} and 1343.68 and 1582.94 cm^{-1} . From the spectrum D/G ratio has been calculated by considering the area under

the D and G bands. The D/G ratio of GO and RGO is 1.10 and 0.85. From the D/G integrated ratio formation of the GO and RGO has been confirmed.

3. 10. Fluorescence spectral analysis:

Fluorescence is a spectrochemical method, wherein the molecules of the analyte are excited by an irradiation at a certain wavelength and emit radiation of a different wavelength. The emission spectrum provides information for both qualitative and quantitative analysis.

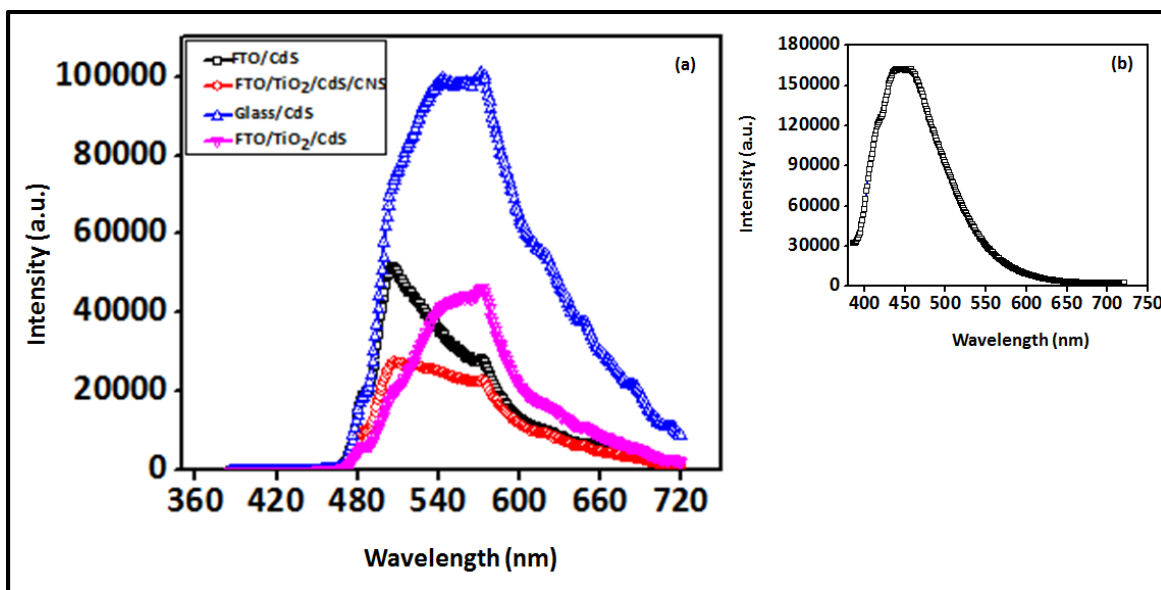


Figure 3.1: (a) A comparative fluorescence spectra of glass/CdS, FTO/CdS, FTO/TiO₂/CdS and FTO/TiO₂/CdS/CNS and (b) the fluorescence spectra of Carbon Nanospheres in ethanol solution obtained at an excitation wavelength of 370 nm. It shows a broad peak from 430 nm to 460 nm range and the intensities of emission peaks are strong.

Table 1:

Composition	Excitation wavelength (nm)	Emission wavelength (nm)	Intensity (a.u.)
Glass/CdS	370	550	100856
FTO/CdS	370	550	51428
FTO/TiO ₂ /CdS	370	550	46069
FTO/TiO ₂ /CdS/CNS	370	550	27746

Photoluminescence (PL) spectra of films were measured on a Horiba Fluoromax-4 fluorescence spectrometer where a suitable filter was utilized during the measurement, and the background correction was also applied. The spectrum of CdS QDs on glass obtained at $\lambda_{\text{ex}} = 370$ nm shows a broad highly asymmetric peak spanning from 477 to 620 nm, indicating it to be composite of multiple components. Deconvolution yielded four peaks: one at 542 nm due to band edge emission and the remaining three components at 502, 571, and 482 nm due to intra gap states. The intensity of the broad peak decreases to 11% of its original value for the TiO₂/CdS/FTO film suggestive of excited electron transfer from the CB of CdS to the CB of TiO₂. Similarly 66% decrease is explained when carbon nanospheres in introduced to the TiO₂/CdS/FTO film.

3. 11. Impedance measurement and determination of back electron transfer for all cells:

The impedance in the intermediate frequencies originates from the charge transfer at the photoanode/S²⁻ interface. The distorted response in the low frequency domain in both electrodes is due to diffusion of the electrolyte species. We fitted the data into an equivalent circuit, shown in Figure 3.m, comprising three resistors and two capacitors for Carbon Nanospheres.

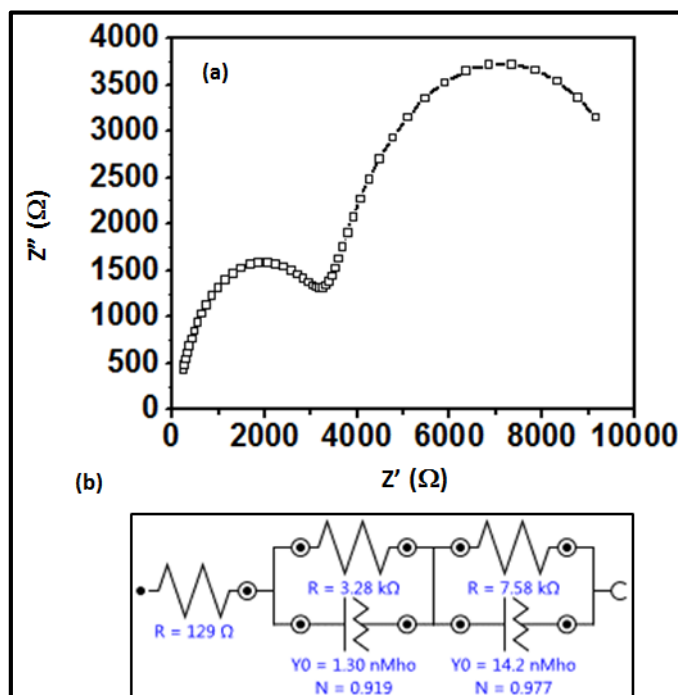


Figure 3.m: (a) Nyquist plots recorded under an ac amplitude of 10 mV for Carbon Nanospheres and (b) The Randles equivalent circuit used for fitting the experimental data.

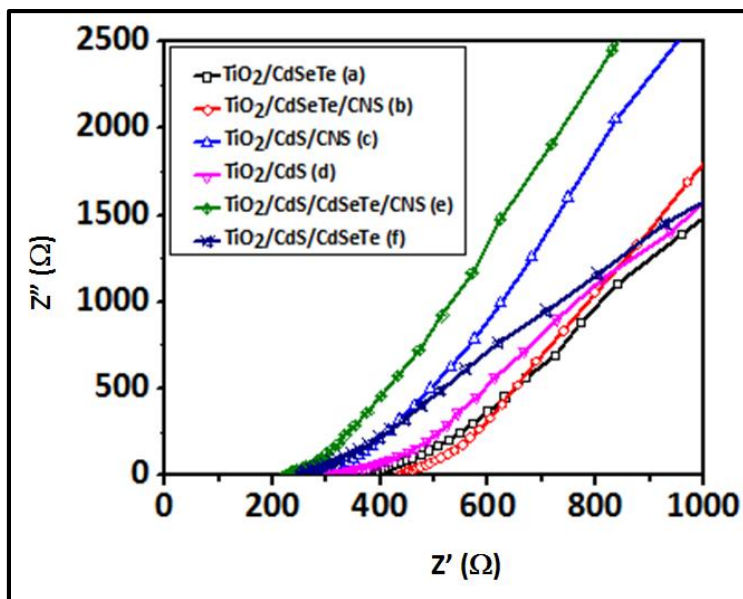


Figure 3.n: Nyquist plots recorded under an ac amplitude of 10 mV, and under V_{OC} for photoelectrochemical solar cells with (a) $TiO_2/CdSeTe$, (b) $TiO_2/CdSeTe/CNS$, (c) $TiO_2/CdS/CNS$, (d) TiO_2/CdS , (e) $TiO_2/CdS/CdSeTe/CNS$, and (f) $TiO_2/CdS/CdSeTe$ as photoanode and Reduced graphene oxide as counter electrode. A 0.1 M Na_2S in ultrapure water-methanol 3:7 (v/v) solution was employed as the electrolyte.

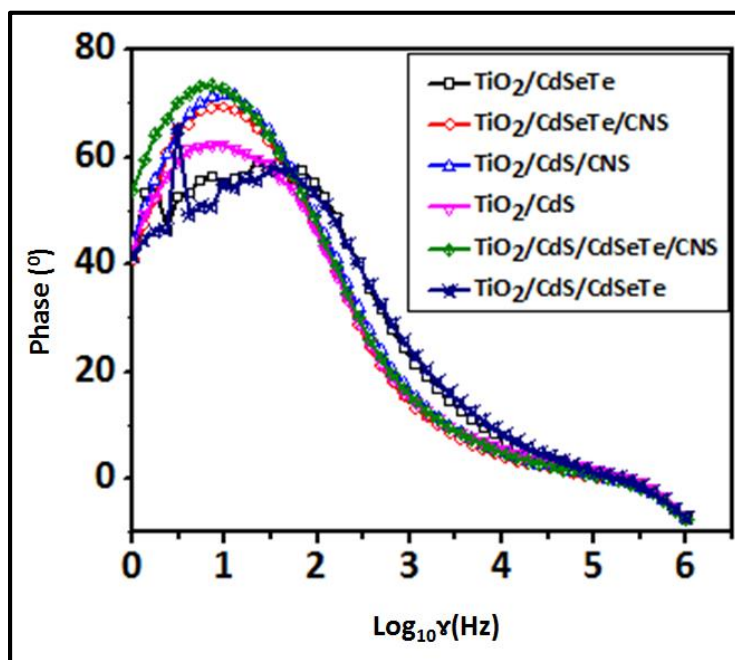


Figure 3.o: A plot of phase vs log of frequency (ν) for all the cells with different photoanode.

By finding the peak value of respective plots, one can find the τ (back electron transfer time) from this simple equation:

$$\tau = 1 / (2\pi\nu) \quad (1)$$

This back electron transfer time and $R_1, R_2, R_3, C_1, C_2, W$ values from Randles equivalent circuit for all the respective cells are provided in a tabular form.

Table 2: Electrochemical Impedance spectroscopy fitting provided parameters of the QDSSCs:

No.	Composition	R_1	R_2	R_3	C_1	C_2	W $\nu_0 = x(\mu$ $Mh_0)$	τ (back electron transfer time; ms)
1	TiO ₂ /CdSeTe	398 Ω	130 Ω	-120 $\mu\Omega$	376nF	758nF	X=12.2	4.01
2	TiO ₂ /CdS/CdSeTe	262 Ω	101 Ω	14.5 $\mu\Omega$	473nF	1.03 μ F	18.8	3.99
3	TiO ₂ /CdS	309 Ω	141 Ω	78.0 $\mu\Omega$	265nF	1.81 μ F	15.9	15.24
4	TiO ₂ /CdS/CNS	291 Ω	116 Ω	52.1 $\mu\Omega$	1.15 μ F	2.43 μ F	11.1	16.50
5	TiO ₂ /CdSeTe/CNS	446 Ω	137 Ω	7.58 Ω	794nF	1.80 μ F	9.36	16.52
6	TiO ₂ /CdS/CdSeTe/ CNS	223 Ω	300 Ω	29.0k Ω	9.92 μ F	5.26 μ F	37.9	21.93

3. 12. Energy Band diagram:

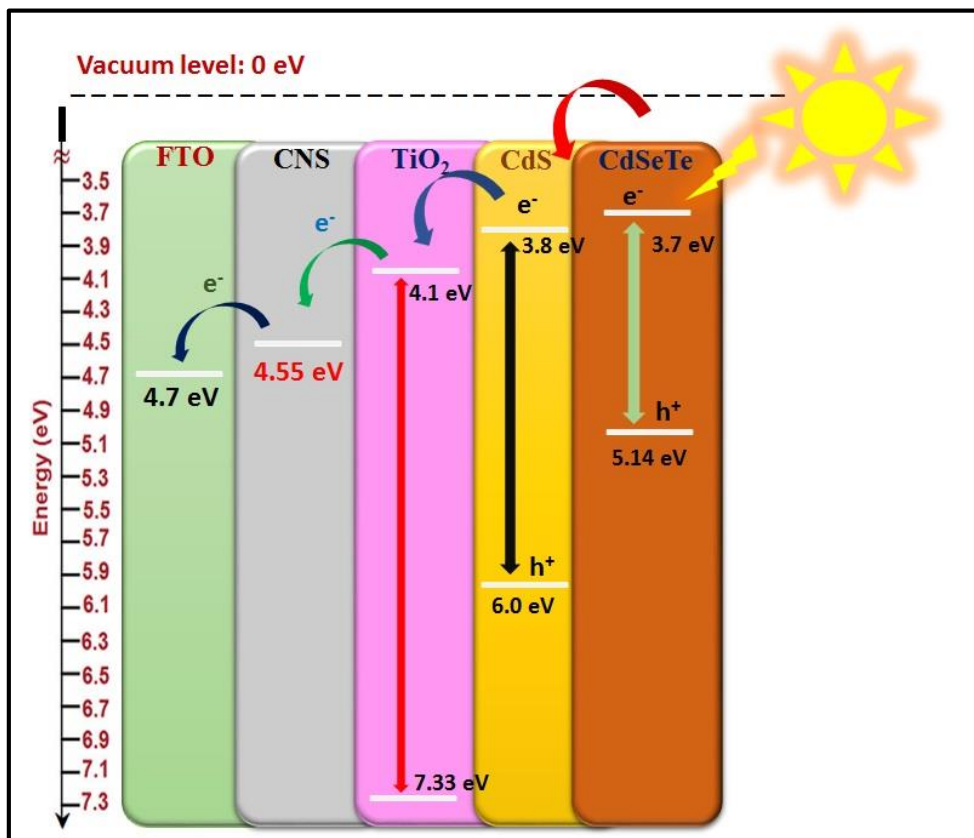


Figure 3.p: Energy band diagram of a FTO/TiO₂/CNS/CdS/CdSeTe photoanode showing the various electron transfer modes.

In the presence of sunlight, there are three different modes of electron transfer process in the CdS-CdSeTe based QDSSCs. Firstly, the electron is excited from the valence band of CdSeTe QD to the conduction band and directly transported to the conduction band of TiO₂ and then to the FTO via the Fermi level of CNS. Secondly, the electron is excited from the valence band of the CdS QD to the conduction band and directly transported to conduction band of TiO₂ and then to FTO via CNS. And finally, an electron is excited from the valence band of CdSeTe QD to the conduction band and directly transported to conduction band of CdS QD injection into the conduction band of TiO₂, and then to FTO via CNS. The whole electrons finally transported through external circuit and taken by the counter electrode (here RGO) and removed to electrolyte, sulfide.

3. 13. J-V characteristics:

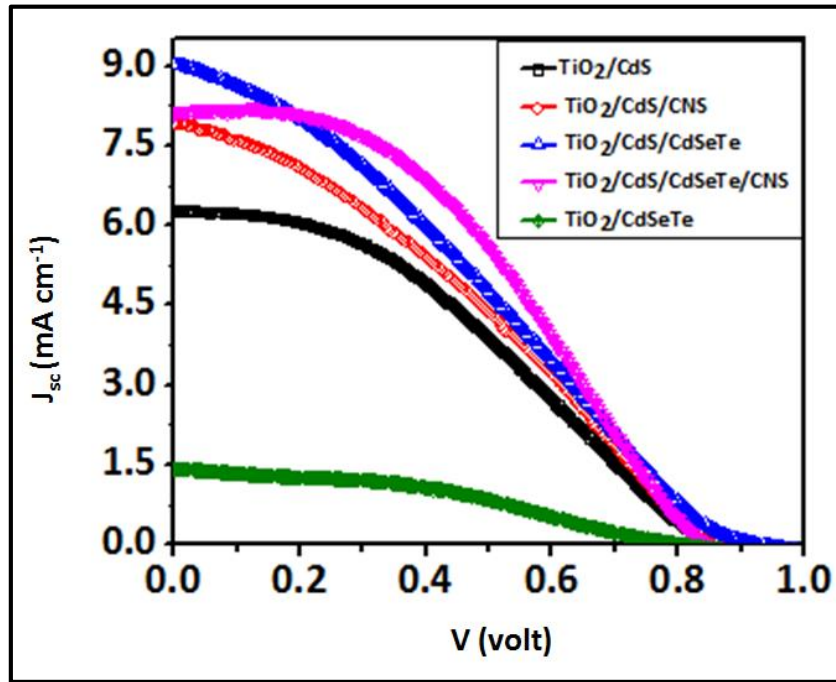


Figure 3.q: The J-V characteristics of TiO_2/CdS , $\text{TiO}_2/\text{CdSeTe}$, $\text{TiO}_2/\text{CdS}/\text{CNS}$, $\text{TiO}_2/\text{CdS}/\text{CdSeTe}$ and $\text{TiO}_2/\text{CdS}/\text{CdSeTe}/\text{CNS}$.

The solar cell parameters for QDSSCs based on different cells are collated in Table 3. The overall power conversion efficiency for the TiO_2/CdS QDs cell is 1.981%, for the $\text{TiO}_2/\text{CdSeTe}$ QDs cell PCE is 0.43%, for the $\text{TiO}_2/\text{CdS}/\text{CNS}$ QDs cell it is 2.21%, for the $\text{TiO}_2/\text{CdS}/\text{CdSeTe}$ QDs cell it is 2.42%, and for the quaternary cell, $\text{TiO}_2/\text{CdS}/\text{CdSeTe}/\text{CNS}$ QDs is 2.821%. The electrolyte was a mixture of 0.1 M Na_2S in dry methanol and water (v/v) electrolyte and reduced graphene oxide (RGO) was used as a counter electrode.

Table 3: Solar cell parameters, QDSSCs prepared in this work:

Photoanode configuration	V_{oc} (mV)	J_{sc} (mA cm^{-2})	Fill factor	η_{best} (%)	η_{avg} (%)
$\text{TiO}_2/\text{CdSeTe}$	0.740	1.39	50.92	0.43	0.3 ± 0.13
TiO_2/CdS	0.881	6.27	35.93	1.986	1.85 ± 0.13
$\text{TiO}_2/\text{CdS}/\text{CNS}$	0.896	7.88	31.29	2.21	2.10 ± 0.11
$\text{TiO}_2/\text{CdS}/\text{CdSeTe}$	0.939	9.02	26.63	2.42	2.38 ± 0.04
$\text{TiO}_2/\text{CdS}/\text{CdSeTe}/\text{CNS}$	0.849	8.14	40.77	2.82	2.65 ± 0.17

4. Conclusion:

A TiO₂/CdS/CdSeTe/CNS assembly was constructed where in the CdS and CdSeTe QDs allows the utilization of both visible and infrared regions of the solar system. Carbon Nanospheres serve as efficient electron acceptors due to a large electrical conductivity (10.36 S cm⁻¹) and a suitable work function. The successful transformation of Graphene oxide to Reduced graphene oxide is confirmed by XRD, SEM and Raman studies. Here Reduced graphene oxide was used as a counter electrode and it worked very efficiently, for cells based on same showed high open circuit voltages, high current densities (J_{sc}) and high fill factors value. The most achievement of this work is the use of Reduced graphene oxide, which is cheaper than that of Carbon cloth or Carbon nanotubes, while at the same time, it shows comparable a work function and high conductivity. The cell based on the TiO₂/CdS/CdSeTe/CNS electrode also delivered a high PCE of 2.82% compared with 1.98% produced by the TiO₂/CdS-based cell when RGO acts as a counter electrode. The optimal solar-cell performance offered by the TiO₂/CdS/CdSeTe/CNS assembly indirectly reflects the synergy between the components of this electrode that permit a high current collection and manifests in high efficiency.

5. References:

- [1]. <http://pveducation.org/>.
- [2]. P. V. Kamat, J. A. Christians, and J. G. Radich, *Langmuir*, 2014, **30** (20), 5716-5725.
- [3]. M. Kouhnavard, S. Ikeda, N. A. Ludin, N. B. Ahmad Khairudin, B. V. Ghaffari, M. A. Mat-Teridi, M. A. Ibrahim, S. Sepeai, and K. Sopian, *Renew. Sustain. Energy Rev.*, 2014, **37**, 397-407.
- [4]. P. A. Basore, *Prog. Photovolt: Res. Appl.*, 1994, **2**, 177-179.
- [5]. K. Ramanathan, M. A. Contreras, C. L. Perkins, S. Asher, F. S. Hasoon, J. Keane, D. Young, M. Romero, W. Metzger, R. Noufi, J. Ward and A. Duda, *Prog. Photovolt: Res. Appl.*, 2003, **11**, 225–230.
- [6]. E. Wang, Z. Ma, Z. Zhang, K. Vandewal, P. Henriksson, O. Inganas, F. Zhang, and M. R. Andersson, *J. Am. Chem. Soc.*, 2011, **133**, 14244-14247.
- [7]. B. O'Regan and M. Gratzel, *Nature*, 1991, **353**, 737-743.

- [8]. Q. Zhang, D. Myers, J. Lan, S. A. Jenekhebc and G. Cao, *Phys. Chem. Chem. Phys.*, 2012, **14**, 14982–14998.
- [9]. <http://www.doityourself.com/stry/6-advantages-of-using-dyesensitized-solar-cells#b>.
- [10]. H. K. Jun, M. A. Careem, and A. K. Arof, *Renew. Sustain. Energy Rev.*, 2013, **22**, 148-167.
- [11]. Nanochemistry, A chemical approach of nanomaterials, G. A. Ozin, A. C. Arsenault, L. Cademartiri, 2009, 2nd Edition, RSC Publishing.
- [12]. A.D. Yoffe, *Adv. Phys.*, 2002, **51**,799.
- [13]. S. M. Shauddin, *Energy and Power*, 2013, **3**, 91-105.
- [14]. J. Luo, L. Ma, T. He, C. F. Ng, S. Wang, H. Sun, and H. J. Fan, *J. Phys. Chem. C*, 2012, **116**, 11956-11963.
- [15]. P. V. Kamat, *J. Phys. Chem. Lett.*, 2013, **4**, 908-918.
- [16]. H. Lee, M. Wang, P. Chen, D. R. Gamelin, S. M. Zakeeruddin, M. Gratzel and Md. K. Nazeeruddin, *Nano Lett.*, 2009, **9**, 4221-4227.
- [17]. C.-F.Chi, Y.-L. Lee and H.-S.Weng, *Nanotechnology*, 2008, **19**, 125704-125705.
- [18]. R. E. Bailey and S. Nie, *J. Am. Chem. Soc*, 2003, **125**, 7100-7106.
- [19]. Z. Yang, C. Chen, P. Roy and H.-S. Chang, *Chem. Commun.*, 2011, **47**, 9561-9571.
- [20]. Z. Pan, K. Zhao, J. Wang, Hu Zhang, Yaoyu Feng, and Xinhua Zhong, *ACS Nano*, 2013, **7**, 5215-5222.
- [21]. B. Zhang, X. Qin, G. R. Li and X. P. Gao, *Energy Environ. Sci.*, 2010, **3**, 1531-1537.
- [22]. S. Bose, T. Kuila, Md. E. Uddin, N. H. Kim, A. K.T. Lau and J. H. Lee, *Polymer*, 2010, **51**, 5921-5928.
- [23]. P. N. Kumar, M. Deepa and A. K. Srivastava, *J. Mater. Chem. A*, 2014, **2**, 9771.
- [24]. G. E. J. Poinern, S. Brundavanam, M. Shah, I. Laava, and D. Fawcett, *Nanotech. Sci. Appl.*, 2012, **5**, 49–59.